COMPUTER SIMULATION OF FUNCTIONAL MATERIALS FOR THERAPEUTIC ULTRASOUND APPLICATIONS

by

SHEIKH JAMIL AHMED

A thesis submitted to the

faculty of graduate studies

Lakehead University

In partial fulfilment of the

requirements for the degree of

Master of Science in Physics

Department of Physics

Lakehead University

August 2013

Thunder Bay Ontario

Lakehead
UNIVERSITY

OFFICE OF GRADUATE STUDIES

NAME OF STUDENT: Sheikh Jamil Ahmed

DEGREE AWARDED: Master of Science in Physics

ACADEMIC UNIT: Faculty of Science and Environmental Studies

TITLE OF THESIS: Computer simulation of functional materials for therapeutic ultrasound applications

This thesis has been prepared

under my supervision

and the candidate has complied

with the Master's regulations.

Signature of Supervisor

14 Sept. 2013

Date

Abstract

Magnetic resonance imaging guided high intensity focused ultrasound is a potential non-invasive treatment which uses constructive interference patterns to concentrate ultrasound energy generated by a piezoelectric (ferroelectric) transducer to thermally ablate affected tumor and cancerous tissues. However, currently used actuators (ultrasound generators) suffer from heating of the ferroelectric materials during operation which causes the dampening of ultrasound by changing the effective thickness frequency relationship and/or depolarization of the material. The excess thermal energy also contributes to the shorter heating and longer cooling cycle of operation which in turn results in higher treatment cost because of the long operating time. Such heating is caused by an energy loss (dielectric dissipation) that takes place when an alternating electric field is applied to the ferroelectric material to generate the ultrasound waves. The loss is related to the area of the hysteresis loop of the material. The project aims at establishing a framework to reduce the dielectric dissipation in ferroelectric materials during their operation as ultrasound transducers. At the initial stage, to study the associated material characteristics, first principle approaches have been adapted as a method in our research rather than experimental methods which would consume more efforts in terms of equipment, money and time. For the purpose of this study, an all electron density functional package WIEN2k is being used along with the advantage of high performance computing. In order to determine the ferroelectric parameters which are related to the polarization based property of materials, an additional software package, BerryPI has been developed in the framework of our research. The switching of ferroelectric materials which is a

macroscopic effect has been studied at the atomistic level. A microscopic interpretation has been made on the growth of domains which is an essential contributor to the ferroelectric hysteresis loss. The findings of the study can be used as a model to assist in the screening of potential ferroelectric materials for ultrasound transducers. In addition, an energy efficient method to apply the electric field has been proposed that will drive the ferroelectric crystal with optimum power and thus, with reduced dielectric dissipation.

Acknowledgements

I would first like to thank my supervisor Dr. Oleg Rubel for his support, guidance and expertise over the course of my masters study. The values he imparted in me during this period are of highest quality. I also feel myself lucky to have Dr. Samuel Pichardo as my co-supervisor. His expertise in MRgFUS helped me in learning about the treatment and have a basic understanding of the nature of the current challenge. The contribution of Dr. Laura Curiel in giving me technical suggestions during the course of my study guided me a lot in improving myself.

Thanks also goes to my committee member Dr. Gautam Das and Dr. Mark Gallagher for technical suggestions during the committee meetings that helped me a lot to plan my research.

Finally, I would like thank some essential contributors to my Masters study. Jeremy Cole, a co-op student who helped me a lot in programming and graphical works mentioned in chapter 5. Jon Kivinen, Benjamin Zaporzan, David Hassan and Victor Xiao performed all the complicated programmings for `BerryPI` without which my masters work wouldn't be successful.

Dedication

Dedicated to my parents and my grandmother.

Contents

List of Tables

List of Figures

Chapter 1

Introduction

1.1 Magnetic resonance guided high intensity focused ultrasound (MRgFUS)

The recent introduction of ultrasound energy to treat tumors and cancer is being considered as a potential candidate for non invasive surgery [1]. The minimal invasive treatment is known as Magnetic resonance guided high intensity focused ultrasound (MRgFUS) [2]. The treatment utilizes the guidance of magnetic resonance imaging (MRI) to localize the target tumor and monitor the temperature profile of the body during the surgery. MRgFUS relies on the basic principles of conventional ultrasound which involves the generation of acoustic waves by vibrating a piezoelectric material (Fig. 1.1(b)) that can propagate harmlessly through any living tissue. During the surgery, a sufficiently high energy ultrasound beam is brought into a narrow focus at the tumor site (Fig. 1.1(a)). The acoustic energy is then converted into a thermal energy by mechanical absorption at the tissue causing a local rise in temperature

at the tumor site to cause a necrosis (a lesion) [1]. The energy deposition is done without causing any bio-effects to the adjacent healthy tissue. The ability to treat tumor tissue distant from the ultrasound source makes the treatment an attractive option for non invasive surgery.

The thermal ablation process requires controlled monitoring in order to prevent the overheating of healthy tissue. MRI also has the capability of mapping the temperature profile and spatial distribution of tissue [3]. This thermal mapping feature is utilized to monitor the thermal ablation process during the treatment(Fig. 1.1(c)).

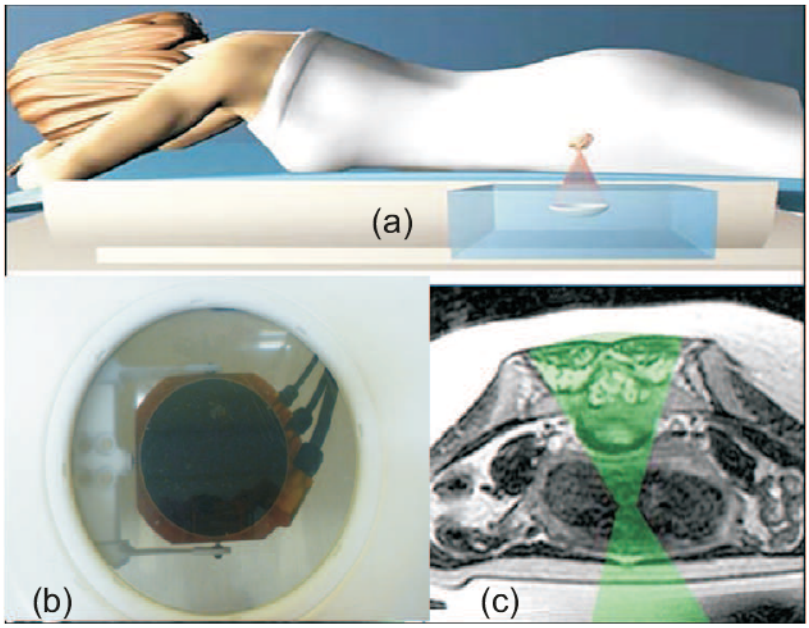

Figure 1.1: Schematics of MRgFUS treatment. (a) Positioning of the patient for treating a tumor in uterine fibroid. (b) The ultrasound transducer which applies the ultrasound energy from underneath the patient. (c) The thermal ablation process is being monitored by MRI ©Department of Radiology, Brigham and Womens Hospital, Harvard Medical School, Boston, Massachusetts [4]

1.2 Basic principles

1.2.1 Therapeutic action

Tissue damage by ultrasound takes place mainly through the conversion of mechanical energy into heat. When the ultrasound beam is focused at the tumor tissue, the energy is converted to heat. Nevertheless, the local temperature rise takes place only if the rate of heating is higher than the heat dissipation rate. MRgFUS aims at causing an irreversible cell death through coagulative necrosis. This is possible by heating the tissue above a threshold temperature of 56^0C for 1 second when thermal toxicity of the cells takes place [1]. Tissue heating is also possible through acoustic cavitation which causes cell necrosis by employing the combined effect of mechanical stress and thermal injury. Here, application of ultrasound causes the tissue to vibrate and subjects the molecular structure to alternative compression and rarefaction. Gas bubbles are formed during the rarefaction stage which either oscillate in size or collapse rapidly causing mechanical stress and a rise in temperature [1].

1.2.2 Ultrasound generation

Ultrasound is sound waves with a frequency greater than the upper limit of human audible range (>20kHz). It propagates in a medium via the vibration of molecules. First, sound waves are generated from a source which initiates vibration. The vibration is then transferred inside the medium to the neighboring molecules. As a result, compression and rarefaction of the medium take place. Compression refers to the state when molecules are pressed or forced together and rarefaction implies the

molecules being weakly bound or free to move (Fig. 1.2). Molecular vibration can take place in both longitudinal (longitudinal wave) and transverse (shear wave) direction. For therapeutic ultrasound purposes, the practice is mostly concentrated in the longitudinal wave, as the shear wave gets attenuated quickly in soft tissues [5–8].

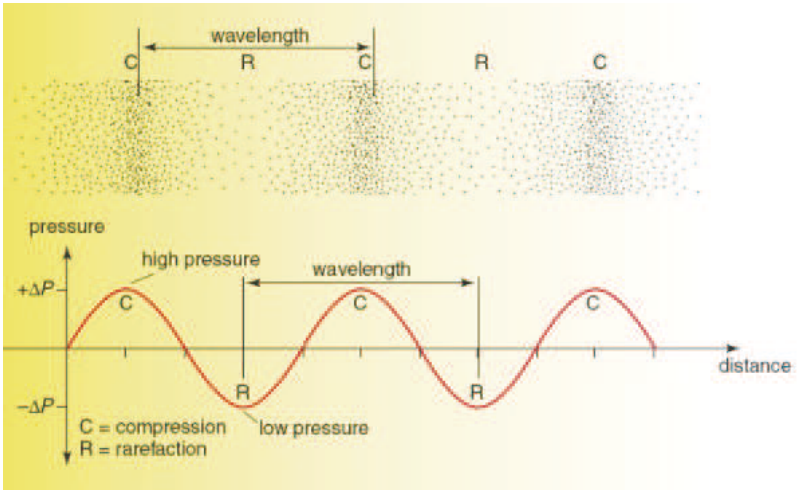

Figure 1.2: Compression and rarefaction of sound waves as they propagate through a medium ©Andrew Simmons [9]

1.2.3 Ultrasound transducer

Ultrasonic transducer is an energy conversion device that converts electrical energy into mechanical energy by the piezoelectric effect. The transducer is operated at the resonance frequency of the piezoelectric material where it demonstrates a very high response to the applied field [10]. The piezoelectric material vibrates by means of rapid contractions and expansions in response to the electrical energy supplied by an alternating electric field. As a consequence, compression and acoustic waves (Fig. 1.2)

are generated [11].

1.2.4 Piezoelectric effect

The phenomenon of piezoelectricity was first discovered by Jacques and Pierre Curie in 1880 when they observed that certain crystals can generate an electric potential [12] under the influence of mechanical stress. Soon after, in 1881 an inverse piezoelectric effect was derived mathematically by Lippman [13] using the thermodynamic principles which was confirmed experimentally by the Curies [14] in the same year. The latter effect is termed as indirect or inverse piezoelectric effect and the former one as direct piezoelectric effect. Such a phenomenon was observed only on certain crystals like tourmaline, quartz, topaz, cane sugar and Rochelle salt in a direction normal to the polar axis only. Based on these observations, it was concluded that the piezoelectric effect can be explained by the symmetry of the crystalline materials and only polar crystals can demonstrate piezoelectricity. Because of its unique behavior, the discovery of piezoelectric materials created great interest among researchers leading these materials to find applications in underwater sonar, medical imaging instruments, car accelerometers, etc [15, 16].

When a perturbation is applied by means of a mechanical stress (direct piezoelectric effect), the resultant mechanical strain alters the equilibrium charge distribution by the rearrangement of charges and constituent atoms. The redistribution of charges produces a net electric potential in the crystal which is expressed by a measurable quantity called polarization. Similarly, during the indirect or converse piezoelectric effect when an electric field is applied to the material, the charge distribution is rear-

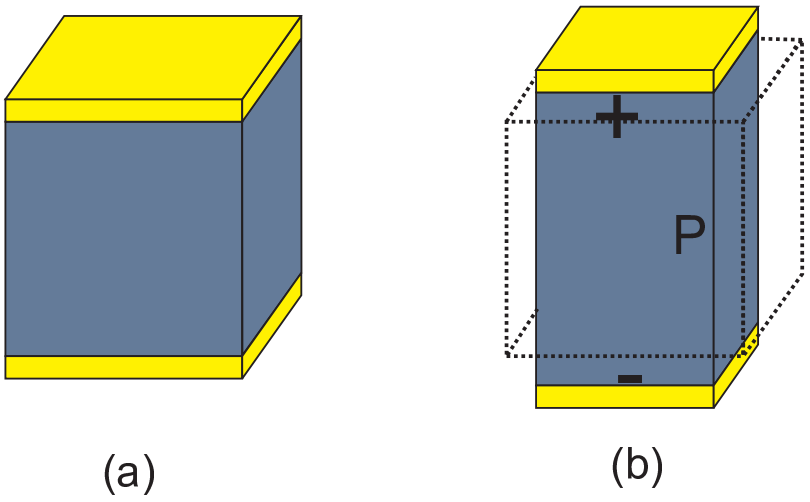

Figure 1.3: (a) A Piezoelectric crystal without any perturbation (mechanical stress or electric field). (b) An external electric field (indirect piezoelectric effect) or mechanical strain (direct piezoelectric effect) will bring the crystal in a piezoelectric state depending on the nature of perturbation

ranged in accordance with the direction and magnitude of the applied electric field. To accommodate this perturbation, a net resultant strain is produced inside the material. However, ferroelectric materials, which are a special class of the piezoelectric group, demonstrate a net polarization under certain temperature conditions without any external perturbation.

1.2.5 Ferroelectricity

Although several crystal classes exhibit a piezoelectric effect, ferroelectric materials are most widely studied due to their exceptional ability of switching between equilibrium states [17–21]. Ferroelectricity was discovered in 1920 while investigating the piezoelectric properties of Rochelle salts [22]. It was observed that these materi-

als demonstrate anomalous dielectric behavior including the presence of a hysteresis (Fig. 1.4) between the applied electric field and the polarization. And also, a sudden change occurs in their piezoelectric behavior under certain temperature conditions.

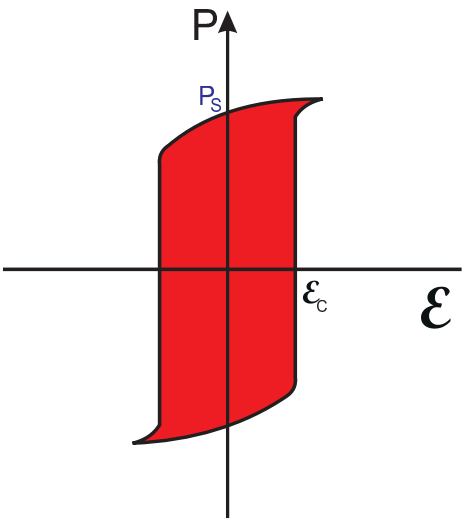

Figure 1.4: The ferroelectric hysteresis showing the polarization response of a ferroelectric material to the applied electric field $\mathcal{E}$

A ferroelectric material is described as an insulating system having multiple equivalent but opposite states of nonzero polarization in the absence of any electric field. The non zero polarization is defined as the **spontaneous polarization**. Such multiple spontaneous polarization states can also be switched amongst each other under the influence of an external electric field. Another interesting property that ferroelectric materials manifest is their ability to inherit several stable structural phases under different temperature conditions. In most common cases, their structural arrangement holds a ferroelectric phase below a characteristic temperature called the Curie temperature, T_c. From the structural symmetry perspective, the material con-

tains lower number of symmetries in the ferroelectric phase with the absence of any inversion symmetry, and as a result, the net charge distribution produces a polar distortion of the structure to generate a nonzero spontaneous polarization. However, if the material is brought to a temperature higher than the Curie temperature, the structure undergoes a transformation from the ferroelectric to the paraelectric state. The paraelectric state is characterized by the presence of a higher degree of symmetry inside the structure balancing the charge distribution in a manner to maintain a zero spontaneous polarization [23, 24].

Since, ferroelectricity is observed in the piezoelectric crystal class, the material must also be polar below the Curie temperature. However, not all polar crystals have the ability to switch their polarization between equivalent and opposite states (i.e., the ability to switch between equivalent atomic configurations). To be considered ferroelectric, the crystal must also demonstrate the switching phenomenon between nonzero polarization states [25]. Figure 1.5(a) shows a 2-dimensional view of a perovskite elementary unit cell in the paraelectric phase. At this stage, the distribution of atoms is highly symmetric which gives rise to a symmetric charge distribution with no net dipole. As a result, the net charge distribution results in a structure with zero polarization. On the other hand, on Fig. 1.5(b), the movement of atoms from their equilibrium position lowers the symmetry and the net charge distribution results in a finite dipole moment along negative Z axis. As a consequence, a spontaneous polarization in that direction confirms that the structure is in a ferroelectric phase. Furthermore, it is also evident from Fig. 1.5(c) that an equivalent but opposite ferroelectric polarization state of the distortion in Fig. 1.5(b) is possible which leads to an equal spontaneous polarization in the positive Z direction. Such a structure

represents the equivalent but opposite ferroelectric state.

According to the conventional theory, the ferroelectric switching phenomenon takes place between the polarization states shown in Fig. 1.5(b) and (c) with an intermediate transition through the paraelectric state (Fig. 1.5(a)). However, achieving such a switching with a structural change requires an external energy to guide the process. For ferroelectric materials, the external energy requirement is given by the energy barrier that the material needs to overcome to undergo the transformation from the ferroelectric to the paraelectric state. The corresponding energy profile as a function of polarization takes a double well shape as shown in Fig. 1.5(d). The external guiding energy is supplied by an alternating electric field which lowers the energy barrier and favors switching between polarization states.

1.3 Material parameters

1.3.1 Piezoelectric charge constant, $\mathbf{d}_{ij}$

The piezoelectric charge constant, d_{ij} measures the response of the piezoelectric (ferroelectric) material to an applied perturbation. For direct piezoelectric effect, it is defined by the polarization, P generated in a particular direction per unit of a directional mechanical stress, $\top$ applied to the material.

$$d_{ij} = \frac{\delta P_i}{\delta \top_j} \tag{1.1}$$

Where, subscript i and j denotes the corresponding directions of response and perturbation. For inverse piezoelectric effect, the charge constant is defined as the mechanical strain, S produced in a particular direction by an electric field, $\mathcal{E}$ applied in

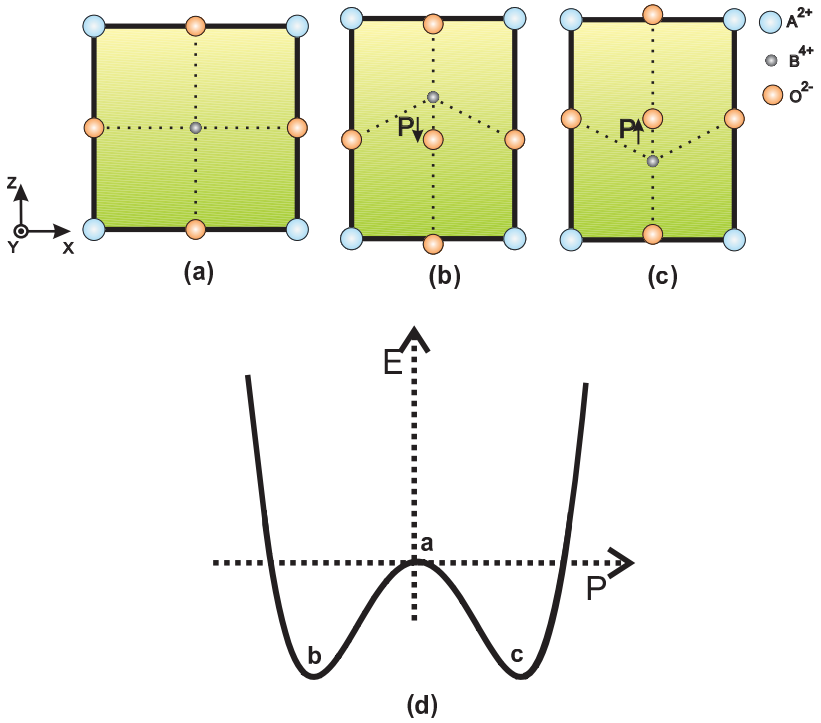

Figure 1.5: Schematics of two dimensional ferroelectric distortion (a) represents a paraelectric state with symmetric charge distribution in all directions which will balance out to give a zero polarization. As the material undergoes a ferroelectric distortion the net charge distribution gives a non zero spontaneous polarization which can be present in either positive (arrow up) state (b) or negative (arrow down) state (c). Ferroelectric switching between the two states of polarization ((a) and (b)) takes place by overcoming an energy barrier

certain direction as depicted by the following expression,

$$d_{ij} = \frac{\delta S_i}{\delta \mathcal{E}_j} \tag{1.2}$$

1.3.2 Electromechanical coupling factor, $\mathbf{k}_{ij}^2$

The electromechanical coupling coefficient indicates the energy conversion efficiency of the material. For inverse piezoelectric effect, it is the ratio between stored mechanical energy and total input electrical energy.

1.3.3 Dielectric constant, ε_{ij}

Dielectric constant is a measure of the electrical energy stored in the material in response to an applied field, $\mathcal{E}$. The electrical energy storage is related to change in polarization with per unit electric field applied leading to the following expression for dielectric constant,

$$\varepsilon_{ij} = \delta_{ij} + \frac{dP_i}{\varepsilon_0 \, d\mathcal{E}_j} \tag{1.3}$$

where, δ_{ij} is the Kronecker delta function which takes a value of 1 only when $i = j$. For $i \neq j$, δ_{ij} is zero and ε_0 is the permittivity in vacuum.

1.3.4 Dielectric dissipation factor, $\tan\delta$

Dielectric dissipation factor expresses the parasitic loss that results by subjecting a material to alternating electric field. It is a measure of dielectric loss of the materials.

As shown in Fig. 1.6, when an electric field, $\mathcal{E}$ is applied to an ideal dielectric material, the resultant charging current find itself out phase by 90^0 with the applied

electric field. However, in a real ferroelectric material, the current also has a loss component in phase with applied electric field and the net resultant current makes an angle δ with the ideal charging current. This loss current is a result of the dissipation of energy as heat. This loss can be interpreted using the parameter tanδ which is the ratio of loss current, *I"* and charging current, *I'*. [26].

$$\tan\delta = \frac{I"}{I'} \tag{1.4}$$

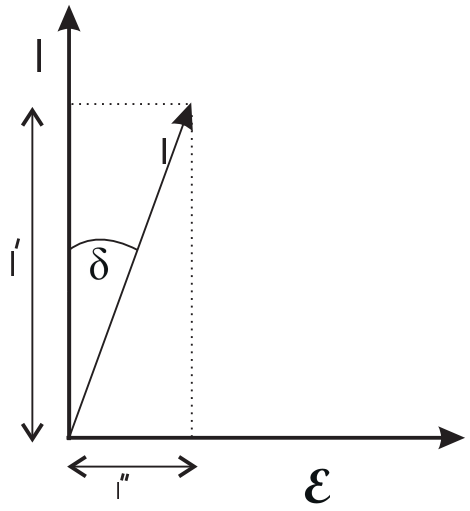

Figure 1.6: The behavior of current in response to an applied electric field $\mathcal{E}$, where I represent real current with a deviation from ideal 90^0 phase between I and V

For ultrasound generation, the electric field is applied in the direction of ferroelectric distortion, and the response of the material is also measured in the same direction. The associated properties are denoted using the subscript 33 (d_33, k_33 for example) Table 1.1 shows the piezoelectric parameters in the ferroelectric distortion

direction for PZT-5H, the material that is currently used for MRgFUS treatment using ultrasound.

Table 1.1: PZT ferroelectric properties

Crystal	$d_{33}(pC/N)$	k_{ij}^2	$\varepsilon_{33}/\varepsilon_0$	$\tan\delta(\%)$
PZT-5H	593 [27]	0.57 [28]	3400 [27]	0.02 [28]

1.4 Current challenge

Despite being a potentially non-invasive treatment, MRgFUS suffers from certain drawbacks. One of the major challenges from the transducer point of view that arises during the operation of an ultrasound transducer is the overheating of the ferroelectric material by excessive thermal build up. Thermal rise can cause the expansion of the ferroelectric materials, and as a result, the effective thickness-resonance frequency relationship is not maintained which results in a dampening of the ultrasound waves. In addition, excessive thermal build up can cause depolarization of the ferroelectric material if the temperature approaches the Curie temperature of the material. The amount of thermal rise increases with an increase in the applied input electrical energy. Such thermal rise thus limits the application of MRgFUS to treat tumors buried deep in the tissue. The limitation arises because treatment of such a tumor requires an ultrasound beam of very high input electrical energy so that it can propagate deep inside the thick layer of tissue. However, excessive thermal build up at high input electrical power makes such a treatment unfeasible. Also, this thermal build up

during the sonication in the near field region of tissue can cause much discomfort to the patient because of their exposure close to the transducer.

Another major drawback in MRgFUS treatment is high treatment cost. The majority of the cost comes from the of MRI [29] which costs about $1000 per hour. For a typical MRgFUS treatment, the operation lasts more than $2-3$ hours which makes the treatment cost more than $3000 in addition to other miscellaneous costs of treatment. The longer operation time is required because of a delay between sonication heating pulses. The delay is caused by two major factors: (i) thermal dissipation of the heat accumulated in the near-field region of the tissue and (ii) dissipation of the excess heat generated in the transducer due to the dielectric dissipation. Figure 1.7 depicts a typical heating and delay cycle [30–32] applied during MRgFUS operation which indicates a time utilization efficiency of approximately 30%.

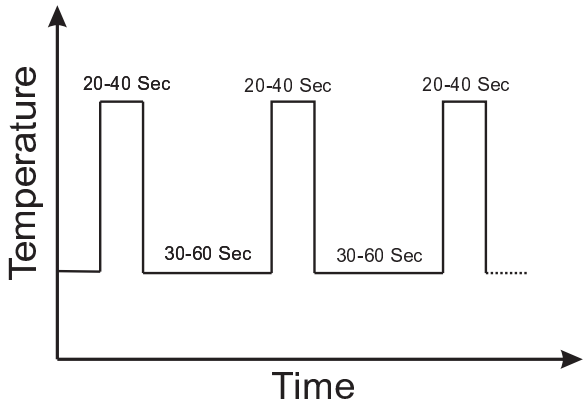

Figure 1.7: Heating and delay cycle in MRgFUS treatment

1.4.1 Dielectric dissipation by hysteresis loss

Heating of the ferroelectric material during the sonication is a fundamental material dependant characteristic [33, 34] which is caused by the ferroelectric loss due to dielectric dissipation inside the crystal. The loss originates from a delay in response of the polarization in the ferroelectric material to the applied field [26]. Normally, the operation of an ultrasound actuator involves the application of alternating electric field to a ferroelectric material with frequency in the MHz range which implies that the polarization reverses $\sim 10^6$ times per seconds for each switching cycle. However, the polarization requires much longer time to attain its equilibrium state with the electric field [26]. As a result, a lag is generated between the applied electric field and polarization. Mathematically, in phasor representation the applied alternating electric field has the following form [33],

$$\mathcal{E} = \mathcal{E}_0 e^{i\omega t} \tag{1.5}$$

where, $\mathcal{E}_0$ is the peak amplitude of the applied electric field. t is time, and ω is the angular frequency. The resultant polarization, P with a peak polarization P_0 acquires a lag of δ in response taking the following form [33],

$$P = P_0 e^{i\omega t - \delta} \tag{1.6}$$

As a result of this delay, the polarization vs electric field curve takes a hysteretic form (Fig. 1.8). Under ideal conditions with no lag, the polarization will change in a linear manner with the applied electric field as shown by the dotted line in Fig. 1.8. As a result, there will be no hysteresis loss in such a system. The loss in the ferroelectric material can be depicted by the shaded colored area shown in Fig. 1.8. Such energy

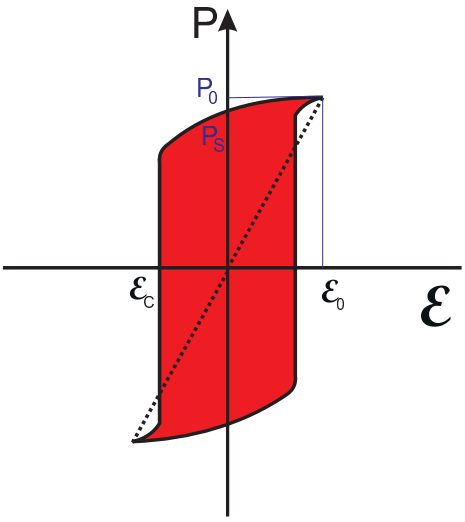

Figure 1.8: Ideal switching with no energy loss assumes a linear relationship between polarization and applied electric field(Dotted line). For ferroelectric material the relationship between polarization and applied electric field takes a hysteresis form.

loss due to hysteresis is converted into heat and results in the heating of the materials during the operation cycle [17, 33].

1.4.2 Research goal

Several studies have been performed on ferroelectric crystals to understand the phenomenon of excessive overheating in these materials. Most of those studies have concentrated at a macroscopic level focusing mainly on growth conditions and alloying [33–42]. Nevertheless, recent development in high performance computing has allowed researchers to apply atomistic level simulations to understand the ferroelectric overheating phenomenon at the atomic level [43–46]. Some atomistic level studies have been performed only by considering forces acting on atoms (molecular dynamics) which did not take all the necessary electronic interactions into consideration [47, 48].

There has also been some studies at the atomistic level that reveal the formation of domain walls in ferroelectric materials [49–51]. However, a limited amount of research exists that focuses on understanding the phenomenon of switching and thus, the dielectric dissipation at an atomistic level using a model that includes all the possible important electronic interactions.

The central aim of this study is to reduce the excessive heating in ferroelectric materials during MRgFUS operation. Achieving such a goal can ensure less ultrasound dampening, depolarization risk and driving the transducer with less input energy demand because of the reduction in losses due to dissipation. Thermal build up reduction will also assist in cutting down the treatment cost as a result of optimized transducer cooling time. Such research can be approached from two different directions. Establishing a basis that will serve as a method in screening of potential materials with a smaller dielectric dissipation factor, $\tan\delta$ can be one of the approaches. Another way this issue can be advanced is by developing a method to operate the existing ferroelectric materials in a manner that optimizes input energy is supplied and reduces dielectric dissipation. Both these approaches have been adopted in the present work and will be discussed in the following chapters.

In chapter 2, we first select a suitable method that includes all the necessary interactions required to advance the ferroelectric overheating issue and then we describe the theoretical formalism behind the selected method.

In chapter 3, we report an important extension to our selected tool, WIEN2k, that enables the calculation of polarization related physical properties of solids. We believe that with this addition, we can further advance our goal of MRgFUS treatment with reduced dielectric dissipation. Our extension will become a useful research tool for

the WIEN2k community as well, which presently stands at 2,000 research groups worldwide.

Chapter 4 deals with a full polarization reversal study over an entire structure of $BaTiO_3$ using first-principles. The work captures the energetic justification for domain wall formation, energetically expensive nucleation phase as well as the relatively easier propagation phase of the domain wall motion. The model opens an opportunity for the computation of domain wall motion dependent properties of ferroelectric materials using first principles. We believe our study will facilitate the design of novel ferroelectric materials by predictive modelling of their physical properties.

In chapter 5, a 3-dimensional potential profile study between multiple possible states of polarization has been performed. Application of an electric field on the surface revealed the ideal polarization switching path. The study then proposes an optimum electric field cycle that can operate the ferroelectric crystal with reduced power which in turn will result in a significant reduction in loss and excessive heating of the ferroelectric material.

Chapter 2

METHOD

2.1 Selection of method

One of the goals of the project is to establish a correlation between structure and dielectric dissipation of ferroelectric materials. Previous formability database studies [52–55] predicted a large number of possible ferroelectric compounds that can be formed. Design of functional ferroelectric materials for a particular practical application with the conventional trial and error approach, therefore, involves study of each of these individual compounds separately. Such a screening process becomes challenging in terms of consumption of time and money. Also, meeting the goal of driving a ferroelectric crystal energy efficiently requires understanding of the switching of polarization states from an atomistic scale. Such knowledge can assist in proposing a ferroelectric switching process that ensures a reduction in the excessive heating of the ferroelectric material. The application of a theoretical approach to address these issues has been highly recognized recently [43–46]. Density functional theory (DFT)

is the most successful and widely used theoretical approach to compute electronic properties of materials using approximate solutions of the Schrödinger equation. The application of DFT in conjunction with crystallographic database information can facilitate the computation of the desired material properties at an atomistic level with a reasonable balance between accuracy and scalability. Such an approach will act as a guide in establishing a basis for reducing the dielectric dissipation of the ferroelectric material. A well-established basis can then benefit experimentalists, who are the essential contributors in any materials design process and thus speed up the process with a higher chance of success.

2.2 Formalism of density functional theory (DFT)

A solid can be described as a system of light, negatively charged electrons and heavy, positively charged nuclei interacting with each other. If the system contains N nuclei each with charge Z_i, then $N + \sum_i^N Z_i$ electromagnetic interacting particles will define the physical properties of that system. The Hamiltonian H of the system unambiguously describes these Coulombic electrostatic interactions between atomic nuclei and electrons. It can be written as

$$H(\mathbf{R}, \mathbf{r}) = T_i(\mathbf{R}) + U_{ii}(\mathbf{R}) + T_e(\mathbf{r}) + U_{ee}(\mathbf{r}) + U_{ie}(\mathbf{R}, \mathbf{r}) \tag{2.1}$$

$T_i(\mathbf{R})$ is the kinetic energy operator for the nuclei and $U_{ii}(\mathbf{R})$ is the potential energy operator that describes nuclei-nuclei interactions. $T_e(\mathbf{r})$ and $U_{ee}(\mathbf{r})$ are the corresponding kinetic energy and potential energy operator for electrons, respectively. The $U_{ie}(\mathbf{r}, \mathbf{R})$ operator represents the external potential or the potential energy due to

the interaction of electrons with the nuclei. $\mathbf{R}=\{\mathbf{R}_n, n=1,...,K\}$ is a set of nuclear coordinates and $\mathbf{r}=\{\mathbf{r}_i, n=1,...,N\}$ corresponds to the electronic coordinates.

The terms appearing in Eq. (2.1) have the following explicit form [56],

$$T_i(\mathbf{R}) = -\sum_{n=1}^{K} \frac{\hbar^2}{2M_n}\Delta_n^2 \tag{2.2}$$

$$U_{ii}(\mathbf{R}) = \frac{1}{8\pi\epsilon_0}\sum_{n=1}^{K}\sum_{n'\neq n}^{K} \frac{Z_n Z_{n'} e^2}{|\mathbf{R}_n - \mathbf{R}_{n'}|} \tag{2.3}$$

$$T_e(\mathbf{r}) = -\sum_{i=1}^{N} \frac{\hbar^2}{2m_0}\Delta_i^2 \tag{2.4}$$

$$U_{ee}(\mathbf{r}) = \frac{1}{8\pi\epsilon_0}\sum_{i=1}^{N}\sum_{j\neq i}^{N} \frac{e^2}{|\mathbf{r}_i - \mathbf{r}_j|} \tag{2.5}$$

$$U_{ie}(\mathbf{r},\mathbf{R}) = -\frac{1}{4\pi\epsilon_0}\sum_{i=1}^{N}\sum_{n=1}^{K} \frac{Z_n e^2}{|\mathbf{r}_i - \mathbf{R}_n|} \tag{2.6}$$

For a given system, if all the components of the Hamiltonian in Eq. (2.1) are provided, the properties of the system can be determined by solving the corresponding many-body Schrödinger equation,

$$H\Psi(\mathbf{R},\mathbf{r}) = E\Psi(\mathbf{R},\mathbf{r}) \tag{2.7}$$

where E is the energy eigenvalue and $\Psi(\mathbf{R},\mathbf{r})$ is the corresponding eigenstate or the wave function.

Solving Eq. (2.7) in practice is almost impossible within full quantum mechanical framework as it implies that both the electrons and nuclei move. One of the complications for the full treatment of Eq. (2.7) is that it requires knowledge of the locations of the nuclei for each particular state of electron motion. The **Born-Openheimer approximation** [57] was introduced to deal with this issue. This approximation

simplifies Eq. (2.7) by considering nuclei as stationary and thus decoupling nuclei and electron dynamics. The assumption is originated from the massiveness of the nuclei in comparison to electrons which also implies that the nuclei are much slower than electrons (i.e., the kinetic energy of the nuclei is negligible in comparison to the kinetic energy of the electron). The application of the Born-Openheimer approximation to the Hamiltonian in Eq. (2.1) therefore eliminates the kinetic energy operator for nuclei, ($T_i(\mathbf{R})$). The potential energy operator for nuclei, $U_{ii}(\mathbf{R})$ also disappears as it becomes constant. The Hamiltonian thus simplifies to

$$H_{BO}(\mathbf{R}, \mathbf{r}) = T_e(\mathbf{r}) + U_{ee}(\mathbf{r}) + U_{ie}(\mathbf{r}, \mathbf{R}) \tag{2.8}$$

The Hamiltonian with fixed nuclei in Eq. (2.8) is much simpler than its original form Eq. (2.1). However, for a many-electron system, it is still almost impossible to solve the electronic wave functions with the Born-Openheimer approximation only as it involves treating massive number of degrees of freedoms that arise from the electron-electron interaction term in Eq. (2.8). The treatment of the term U_{ee} for an electron in a particular state of electronic motion requires information about the locations of all other electrons due the influence of the electron under consideration. Such adjustment of positions by all the electrons to treat every single electron introduces a massive number of variables in Eq. (2.8) which is almost impossible to solve without further simplification.

Hartree in 1928 [58], proposed a theory that simplifies the electron-electron interaction term in Eq. (2.8). The theory considers the interaction of electrons with the average over potential of other electrons. The introduction of the Hartree theory thus brought the Hamiltonian in Eq. (2.8) into a consideration in a non-interacting

system. The potential energy due to electronic interactions according to the Hartree theory is given by

$$U_{Hartree} = \frac{e^2}{4\pi\epsilon_0} \int \frac{\rho(\mathbf{r}')}{|\mathbf{r} - \mathbf{r}'|} d\mathbf{r}' \,, \tag{2.9}$$

where $\rho(\mathbf{r}')$ is the average electron density at position $\mathbf{r}'$. For a system with N electrons, the ground-state density is expressed as,

$$\rho(\mathbf{r}') = \sum_{j=1}^{N} |\Psi_j(\mathbf{r}')|^2 \tag{2.10}$$

The single-particle Schrödinger equation according to the Hartree theory takes the following form,

$$\left[-\frac{\hbar^2}{2m}\nabla^2 + U_{ie}(\mathbf{r}) + U_{Hartree}(\mathbf{r}) \right] \Psi_i(\mathbf{r}) = \epsilon_i \Psi_i(\mathbf{r}) \,, \tag{2.11}$$

where i and j represent quantum numbers for the single-particle state.

The Hartree theory, however, is not consistent with the Pauli exclusion principle [59]. Based on the Pauli exclusion principle, a many-electron wave function must satisfy the Schrödinger equation and be antisymmetric [59]. Although the wave function Ψ in the Hartree theory satisfy the Schrödinger equation, it is not antisymmetric. The Hartree potential term, as a result, contains coupling between orbital i and itself as the orbital is already included in the total charge density ρ. However, an electron can not interact with itself. To address this shortcoming in the Hartree theory, Fock introduced [60] an additional term in the Hartree Schrödinger equation. This **Hartree-Fock theory** takes the antisymmetry of many-electron wave function fully into account and therefore satisfies the Pauli exclusion principle:

$$\left[-\frac{\hbar^2}{2m}\nabla^2 + U_{ie}(\mathbf{r}) + U_{Hartree}(\mathbf{r})\right]\Psi_i(\mathbf{r}) - \frac{e^2}{4\pi\epsilon_0}\sum_{j=1}^{N}\int d\mathbf{r}'\frac{1}{|\mathbf{r}-\mathbf{r}'|}\Psi_j(\mathbf{r}')^*\Psi_i(\mathbf{r}')\Psi_j(\mathbf{r})\delta_{\sigma_i\sigma_j} = \epsilon_i\Psi_i(\mathbf{r})\,. \tag{2.12}$$

where $\delta_{\sigma_i\sigma_j}$ denotes the Kronecker delta function with σ_i and σ_j as spin orbital levels.

The total energy of the system is minimized in terms of trial wave functions using the **mean field theory** which is based on Rayleigh-Ritz's variational principle [61–63]. The HF theory uses the Slater determinant consisting of all possible permutations of two sets of single-particle coordinates exchanged $\{\mathbf{r}_i, \sigma_i\}$, which is antisymmetric under exchange of any two particles, as its trial wave function. The Hartree theory corresponds to a trial wave function which is a simple product of N single-particle wave functions.

Application of the Hartree-Fock theory enables the computation of energies for a static configuration of a many-electron system. However, the theory does not fully account for the correlation among electrons (only the Pauli exclusion principle is fulfilled). The electron correlation term becomes significant in heavily interacting systems where Hartree-Fock theory yields unsatisfactory results, therefore, limiting its application to the molecular systems. In addition, the electron orbitals entering the Hartree-Fock equations in a non-local way makes it difficult to be applied to extended systems [64]. A more powerful and modern method that addresses the issue is called the **density functional theory (DFT)**.

DFT is based on two theorems given by Hohenberg and Kohn in 1964 [65].

First theorem: *With a trivial additive constant, the external potential U_{ie} is*

uniquely a functional of the electronic density. This leads to the consequence that the ground-state energy functional is a unique functional of the ground-state density of the system.

The first theorem states that the electronic density of a system contains as much information as the wave function. As a consequence, any ground-state observable quantity can be expressed as a unique functional of the electron density.

Second theorem: *The ground-state energy functional is of the following from,*

$$\begin{aligned} E_{U_{ie}}[\rho] &= \langle \Psi | T_e + U_{ee} | \Psi \rangle + \langle \Psi | U_{ie} | \Psi \rangle \\ &= F_{HK}[\rho] + \int \rho(\mathbf{r})\, U_{ie}(\mathbf{r})\, d\mathbf{r} \end{aligned} \tag{2.13}$$

where $\mathrm{F}_{HK}[\rho]$ is defined as the Hohenberg-Kohn density functional. The functional does not contain any information about the nuclei or their locations. For a given system, knowledge of $\mathrm{F}_{HK}[\rho]$ necessarily implies information on the solution of the full many-body Schrödinger equation. It should be noted that $\mathrm{F}_{HK}[\rho]$ is a functional that does not depend explicitly on the external potential but only on the electronic density. $\mathrm{E}_{U_{ie}}$ represents the ground-state total energy of the system with a ground-state electronic density that corresponds to an external potential, U_{ie}. Application of Rayleigh-Ritz's variational principle [61–63] facilitates the determination of the ground-state density by minimizing the total energy of the system in terms of the trial wave function.

Hohenberg-Kohn theory proposes an unique way of obtaining the ground-state properties of an interacting system. However, the theory does not provide any method for obtaining energy functional, $\mathrm{F}_{HK}[\rho]$. In 1965, Kohn and Sham [66] combined the Hohenberg-Kohn theorem with the early postulate by Hartree and Fock [58, 60] which

turned DFT into a practical tool to study the ground-state properties of materials.

Kohn and Sham expressed the energy functional in the following form:

$$E_{U_{ie}}[\rho] = -\frac{\hbar^2}{2m}\nabla^2[\rho] + U_{Hartree}[\rho] + U_{xc}[\rho] + U_{ie}[\rho]\,, \tag{2.14}$$

where U_{xc} is the exchange correlation functional.

Equation (2.14) thus simplifies the expression for an interacting system by considering it as a non-interacting classical electron gas subjected to an external potential due to the nuclei and then, by the addition of the exchange correlation effects. The corresponding **Kohn-Sham** Hamiltonian takes the form,

$$H_{KS} = -\frac{\hbar^2}{2m}\nabla^2(\mathbf{r}) + U_{Hartree} + U_{xc} + U_{ie} \tag{2.15}$$

DFT aims at solving the Schrödinger equation with the Kohn-Sham Hamiltonian, H_{KS}; for any interacting many-electron system. Majority of the electronic structure calculations for solids are performed within this first principle framework.

2.3 Exchange correlation functional

There are several schemes to apply exchange correlation functionals in DFT. Amongst them, two of the most significant and most widely used are called the local density approximation (LDA) and the generalized gradient approximation (GGA). These two functionals have been adopted in various case studies throughout the present work.

2.3.1 Local-density approximation (LDA)

LDA defines the exchange correlation energy $U_{xc}(\mathbf{r})$ of a non-homogenous system by first dividing the system into infinitesimally small volumes with constant density [67–

69]. Then, it assumes that for each of those volumes, the exchange correlation energy per electron at a particular point $\mathbf{r}$ is equal to the exchange correlation energy per electron of a homogenous gas that has the same electronic density as the system in question. The expression takes the form [69],

$$U_{xc}[\rho(\mathbf{r})] = \int \upsilon_{xc}^{homogenous}[\rho(\mathbf{r})]\rho(\mathbf{r})d\mathbf{r} \tag{2.16}$$

where $\upsilon_{xc}^{homogenous}$ is the exchange correlation energy per electron for the system as a homogenous gas.

While treating the system as a homogenous electron gas, the exchange energy is computed using the following expression by Dirac [69, 70],

$$U_x = -\frac{3}{4}\left[\frac{3}{\pi}\rho(\mathbf{r})\right]^{\frac{1}{3}} \tag{2.17}$$

and the correlation energy of the homogeneous gas is estimated from quantum Monte-Carlo simulation of the energy of a homogenous electron gas [67].

LDA performs well in systems where the electronic density is homogenous in comparison to system with non-homogenous electron density [69]. As a consequence, it overestimates binding energy of molecules and cohesive energy for solids. Despite of inaccurate binding energies, LDA reproduces bond lengths and angle properties for systems with strong bonds with fairly high accuracy, which are in good agreement with the experimental results. LDA generally underestimates the bond length slightly [69].

2.3.2 Generalized gradient approximation (GGA)

To address situations when there are inhomogeneities in the electronic density, the GGA exchange correlation functional has been introduced. The basis here relies on

carrying out an expansion of density in terms of the gradient and higher derivatives. The exchange correlation energy takes the following form [69],

$$U_{xc}[\rho(\mathbf{r})] = \int \upsilon_{xc}^{LDA}[\rho(\mathbf{r})]\rho(\mathbf{r})F_{xc}[\rho(\mathbf{r}), \nabla\rho(\mathbf{r}), \nabla^2\rho(\mathbf{r})...]d\mathbf{r} \tag{2.18}$$

Here F_{xc} is an enhancement factor that modifies the LDA expression based on variation of density in the vicinity of the point of interest.

In general, GGA overestimates structural properties such as the bond length.

Several improvements to exchange correlation functionals (exact exchange approach [71], screen exchanged LDA [72], hybrid exchange correlation [73], GW [74]) have been proposed that improve the performance of LDA and GGA. However, implementation of these exchange correlation functionals can be computationally challenging. For ferroelectric crystals, LDA and GGA reproduce experimental structural parameters with fair accuracy ($\sim$6 percent) and are the preferred exchange correlation functionals.

Chapter 3

BerryPI-A package for polarization computation

Before we begin, we need to point out that the current chapter is by and a large reproduction of an article published by the author. [75].

3.1 Introduction

First-principle microscopic theories, such as density functional theory (DFT), play a major role in the development of parameter-free models that establish a relation between atomic structure and material properties using a minimum of or no experimental input at all. Combined with the recent advances in high-performance computing, this development open up new opportunities for exploring novel materials and understanding their properties [76, 77]. In particular, the ability of DFT to capture microscopic polarization [78–80] enables the calculation of the related material properties, such as spontaneous polarization and Born effective charge [79],

permittivity [81], pyroelectric coefficient [82] and piezoelectric tensor [83, 84].

The calculation of polarization using a geometric phase approach (also known as the Berry phase [91]) is now implemented in major solid-state DFT packages, such as `ABINIT` [85] and `VASP` [86], which belong to the plane wave family. To the best of our knowledge, only one successful realization of the Berry phase approach using the all-electron full-potential linearized augmented plane wave (LAPW) method has been reported so far [83]. However, the package is not available for external users.

This chapter presents a new software `BerryPI` that extends the capability of the popular all-electron full-potential DFT package `WIEN2k` [87] to calculation of polarization in solids using the Berry phase approach. `BerryPI` also relies on the `WIEN2WANNIER` [88] program in the computation of overlap matrices as described below. As an example, we calculated the spontaneous polarization and Born effective charges of several perovskite, zinc-blende and rock-salt structures and compare the results with experimental data, pseudopotenial calculations and other DFT results reported in the literature.

3.2 Modern theory of polarization

In any phenomenological description of a dielectric medium, macroscopic polarization is the most essential concept [89]. However, the consideration of polarization for a periodic crystal proved to be a long-standing problem due to lack of proper microscopic understanding [80].

The most well known definition of polarization relies on expressing the quantity in terms of the dipole moment within a unit volume of a finite system [82].

$$\mathbf{P}_{System} = \frac{1}{\mathbf{V}_{System}} \int_{System} d\mathbf{r}\, \mathbf{r}\, \eta(\mathbf{r}) \tag{3.1}$$

where, $\eta(\mathbf{r})$ is the total charge density of a system with volume, $\mathbf{V}_{System}$.

Equation (3.1) is applicable only to a finite macroscopic system which implies the charge density will have contribution from both the surfaces and the bulk. However, these two contributions cannot be easily disentangled. Furthermore, if the surface preparation of the system is altered in a manner that the surface charge density is also changed, the dipole moment scaling also gets shifted. The scaling shift essentially implies a polarization change in the system although the bulk of the system still remains unchanged. The definition thus neglects the contribution from bulk of the system.

Another approach towards the definition describes the polarization of a system with periodic charge distribution by segmenting it into unit cells of volume, Ω and carrying the following integration [82],

$$\mathbf{P}_{Cell} = \frac{1}{\mathbf{\Omega}} \int_{\Omega} d\mathbf{r}\, \mathbf{r}\, \eta(\mathbf{r}) \tag{3.2}$$

The polarization in Eq. (3.2) however, relies heavily on the choice of the elementary cell. As evident from Fig 3.1, a change in the shape and the location of the unit cell in the same charge distribution causes the resultant dipole moments to be in different orientation and thus polarization direction to be different. Equation (3.2) is only applicable to systems that have a cell boundary with zero charge density. However, electronic charge density in crystalline materials is continuous and periodic.

Deficiencies in the previous definitions led to the consideration of this phenomenon from experimental point of view where the change in the polarization is treated as

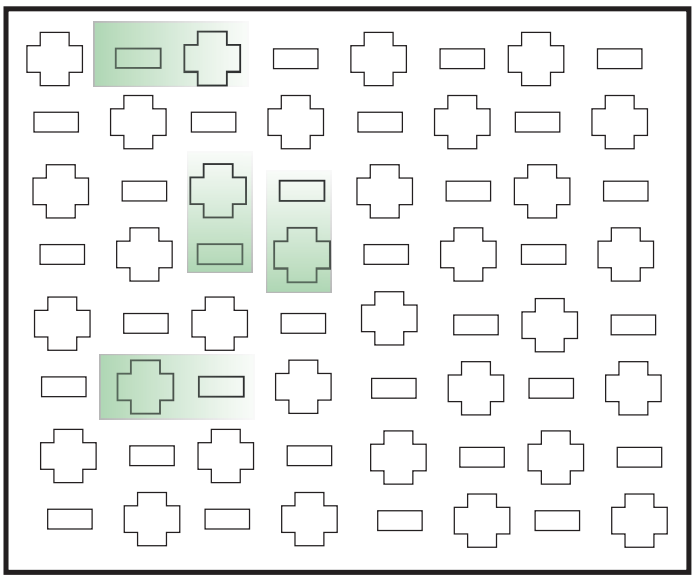

Figure 3.1: The different choices of unit cell yield different estimation of dipole moment (polarization).

a measurable quantity rather than its bulk value. The change in polarization is related to the current flowing through the interior of the system during a time period associated with perturbation. Such consideration can be formulated mathematically as follows [82],

$$\Delta\mathbf{P} = \mathbf{P}^{(1)} - \mathbf{P}^{(0)} = \Omega^{-1} \int dt \int_{\text{cell}} d\mathbf{r} \;\; \mathbf{j}(\mathbf{r}, t) \;, \tag{3.3}$$

where $\mathbf{j}(\mathbf{r}, t)$ is the local transient current density resulting from a charge redistribution inside the bulk unit cell. Electric current flowing through the system can be segmented into ionic and electronic part. The ionic part is associated with the change in ionic phase which is given by the displacement of ions due to electric field or any external perturbation. The electronic current is given by change in electronic phase which represents change in electronic density or average positions of the electrons due to the external perturbation.

Extension of Eq. (3.3) from time dependent parameter to adiabatic perturbation at each time interval λ yields [80, 82, 90],

$$\Delta\mathbf{P} = \mathbf{P}_{\lambda_1} - \mathbf{P}_{\lambda_0} = \int_{\lambda_0}^{\lambda_1} \frac{\delta\mathbf{P}}{\delta\lambda} d\lambda \tag{3.4}$$

Here, λ represents the atomic displacement or strain in response to an external perturbation that transforms the crystal from an initial state λ_0 to a perturbed state λ_1. Such a transformation leads to adiabatic evolution of polarization from $\mathbf{P}_{\lambda_0}$ to $\mathbf{P}_{\lambda_1}$. Equation (3.4) is applicable to any insulating system for which the polarization derivative can be computed along the path $\lambda_0 \longrightarrow \lambda_1$. This phenomenology of expressing polarization in terms of their difference rather than the absolute value is the basis of modern theory of polarization [80, 82].

In the framework of the modern theory, polarization of a given state thus, consists of two components: ionic and electronic

$$\mathbf{P} = \mathbf{P}_{\text{ion}} + \mathbf{P}_{\text{el}} \ . \tag{3.5}$$

Ionic polarization, $\mathbf{P}_{\text{ion}}$ is caused by relative displacement of positive and negative ions in a polar crystal. Computation of ionic polarization is straightforward; it is based on the position of atomic nuclei and the corresponding ionic charges [80]. The electronic part of the polarization is related to the spatial distribution of the electron density [82], which can be expressed in terms of a geometric phase (Berry phase) [78, 91] as explained below.

3.3 Berry phase

Berry phase was introduced by M.V. Berry in 1984 to compute the geometric phase acquired by a quantum system while traversing along a closed path C in parameter space [91]. The parameter space is defined by a set values on which the hamiltonian depends. The Berry phase for a Hamiltonian $H(\Re)$ with parameters $\Re = \{a_1, a_2\}$ can be stated as [92],

$$\mathrm{d}\varphi_n(C) = i \oint_C < n(\Re)|\nabla_{\Re} n(\Re) > d\Re \tag{3.6}$$

Where $\nabla_{\Re}$ is the derivative with respect to $\Re$ and $n(\Re)$ is the eigenstate of $H(\Re)$

For a crystalline material with periodic boundary condition, the reciprocal lattice vector, $\mathbf{k}$ is considered to be the parameter space and the corresponding eigenstate is expressed by the periodic part of bloch wave function, $u_{n\mathbf{k}}$ where n is the band index. Thus the Berry phase then takes the form [80, 82, 91],

$$\mathrm{d}\varphi_n = -i\langle u_{n\mathbf{k}}|\nabla_{\mathbf{k}}|u_{n\mathbf{k}}\rangle \cdot \mathrm{d}\mathbf{k} = -i \ln\langle u_{n\mathbf{k}}|u_{n(\mathbf{k}+\mathrm{d}\mathbf{k})}\rangle \ . \tag{3.7}$$

For a given system in unperturbed state, the Berry phase term in Eq. (3.7) thus computes the electronic phase by applying the periodic boundary condition to perform the closed loop internal. In addition, if an external perturbation is applied to the system the wave function acquires a phase with respect to the unperturbed state. The change in electronic phase yields the change in electronic polarization which is a measure of the electronic component of the current flowing through the system due to the perturbation.

The electronic part of the polarization is related to the average position of electrons. Bolunt et al. [93] showed that the position operator for electrons is related to

the Berry phase according to,

$$\langle \psi_{n\mathbf{k}}(\mathbf{r})|\mathbf{r}|\psi_{n\mathbf{k}}(\mathbf{r})\rangle = \frac{i\,\Omega}{(2\pi)^3}\sum_{n}^{\substack{\text{occ.}\\ \text{bands}}}\int_{\text{BZ}} \mathrm{d}\mathbf{k}\ \langle u_{n\mathbf{k}}|\nabla_{\mathbf{k}}|u_{n\mathbf{k}}\rangle. \tag{3.8}$$

3.4 Method

We consider a periodic insulating crystal, which is represented by a unit cell with N atoms and M doubly-occupied bands (non spin-polarized calculation is considered). It is assumed that the electronic ground state can be described by a single-particle mean-field Hamiltonian as in the density-functional theory. The eigenstates of this Hamiltonian are the Bloch functions

$$\psi_{n\mathbf{k}}(\mathbf{r}) = u_{n\mathbf{k}}(\mathbf{r})\,\mathrm{e}^{i\mathbf{k}\cdot\mathbf{r}}\ , \tag{3.9}$$

which are characterized by the band-index n and the wave vector $\mathbf{k}$. The complex amplitude $u_{n\mathbf{k}}(\mathbf{r}) = u_{n\mathbf{k}}(\mathbf{r}+\mathbf{R})$ remains invariant for any lattice vector $\mathbf{R}$.

The total microscopic polarization of such a system is given by [78]

$$\mathbf{P} = \frac{e}{\Omega}\sum_{s}^{\text{atoms}} Z_s^{\text{ion}}\mathbf{r}_s \ - \ \frac{2ei}{(2\pi)^3}\sum_{n}^{\substack{\text{occ.}\\ \text{bands}}}\int_{\text{BZ}} \mathrm{d}\mathbf{k}\ \langle u_{n\mathbf{k}}|\nabla_{\mathbf{k}}|u_{n\mathbf{k}}\rangle\ , \tag{3.10}$$

where Ω is the simulation cell volume, e is the elementary charge, Z_s^{ion} is the ionic charge represented by the number of valence electrons in the atom s and $\mathbf{r}_s$ is its position vector. The factor of 2 in the numerator corresponds to the band occupancy. The integration in Eq. (3.10) is performed over the Brillouin zone (BZ), and the integrand is closely related to the geometrical phase change as shown in Eq. (3.7)

After summation over all occupied bands, the integral in Eq. (3.10) will represent

an average phase acquired by system wavefunctions, i.e. the electronic phase. This phase value has the uncertainty of an integer multiple of 2π.

The Cartesian α component of total polarization of a state can be expressed in terms of the corresponding total phase Φ_α [84]

$$P_\alpha = \frac{e}{\Omega}\,\frac{\Phi_\alpha}{2\pi}\,R_\alpha \tag{3.11}$$

Where R_α is the length of the real-space lattice vector in the direction α. By analogy with Eq. (3.10) for polarization, the total phase is split into two components

$$\Phi_\alpha = \varphi_{\mathrm{el},\alpha} + \varphi_{\mathrm{ion},\alpha}\ , \tag{3.12}$$

Where $\varphi_{\mathrm{el},\alpha}$ and $\varphi_{\mathrm{ion},\alpha}$ are electronic and ionic phases, respectively.

The ionic phase for a given structure is determined by the spatial position and charge of individual ions via [84]

$$\varphi_{\mathrm{ion},\alpha} = 2\pi \sum_{s=1}^{N} Z_s^{\mathrm{ion}} \rho_{s,\alpha}\ , \qquad \text{wrapped in the range } [0, 2\pi] \tag{3.13}$$

where $\rho_{s,\alpha}$ is the fractional coordinate of ion s in the crystallographic direction α.

In practice, the Berry phase $\varphi(\mathbf{k}_\parallel)$ is computed for individual k-paths parallel to the α-axis in the Brillouin zone (Fig. 3.2), and each result is wrapped in the range of $[0, 2\pi]$. Then, the total electronic phase corresponds to an average [78]

$$\varphi_{\mathrm{el},\alpha} = S_\perp^{-1} \int_{S_\perp} \mathrm{d}S_\perp\ \varphi(\mathbf{k}_\parallel)\ , \tag{3.14}$$

Where $S_\perp$ is the surface area of the Brillouin zone perpendicular to the α-axis. The Berry phase for an individual path $\mathbf{k}_\parallel$ can be expressed as [78]

$$\varphi(\mathbf{k}_\parallel) = 2\ \mathrm{Im}\left[\ln \prod_{j=0}^{J-1} \det \mathbb{S}_{M\times M}(\mathbf{k}_j, \mathbf{k}_{j+1})\right]\ . \tag{3.15}$$

Here $\mathbb{S}$ is the overlap matrix of the size M^2, where M is the number of occupied bands, and the factor of two takes into account the spin degeneracy. The path is designed such that the end k-point represents the starting point displaced by the reciprocal lattice vector, i.e., $k_J - k_0 = G_\alpha$.

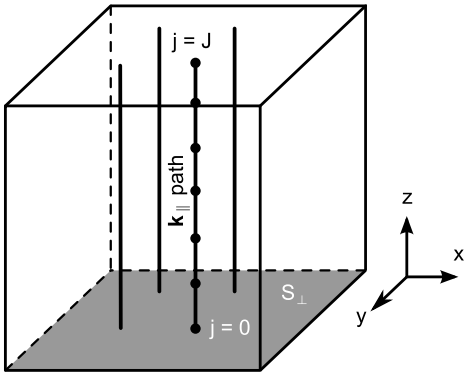

Figure 3.2: Berry phase integration in the Brillouin zone for calculation of the electronic polarization along z-axis.

Computation of the overlap integral between two cell periodic parts of the Bloch function

$$\mathbb{S}_{mn}(\mathbf{k}_j, \mathbf{k}_{j+1}) = \langle u_{m\mathbf{k}_j} | u_{n\mathbf{k}_{j+1}} \rangle \tag{3.16}$$

is the most challenging part in determining the Berry phase. Here m and n refer to the occupied band indices, which span in the range 1 to M. Calculation of such an integral is a part of the standard procedure of constructing Wannier functions, which is done by the `WIEN2WANNIER` package [88].

3.5 Program implementation

`BerryPI` is a Python script that controls the execution process according to the flow in Table 3.1. The script is invoked in the case directory after completing the standard `WIEN2k` self-consistency field cycle. The only input parameter required is the **k**-mesh for Berry phase integration. The script determines the number of occupied bands M, cell geometry, the ionic charges and their relative positions based on `WIEN2k` files. The electronic, ionic and total phases as well as the corresponding components of polarization are calculated along the Cartesian axes.

Since the ionic and electronic phases used in the calculation of polarization carry the uncertainty of an integer multiple of 2π, the proper calculation of the polarization difference between two structures requires $\Delta P \lesssim |eR/\Omega|$. In the case of typical perovskite structures, $|eR/\Omega|$ is of the order of 1 C/m^2, which is still greater than typical values of the spontaneous polarization (see Table 3.3).

When comparing the polarization between two structures, it is useful to inspect the total phases as shown in Fig. 3.3. In this specific case, the phases are $\Phi^{(0)} = -0.9\pi$ and $\Phi^{(1)} = +0.9\pi$, which yields $\Delta\Phi^{(1-0)} = 1.8\pi$ instead of -0.2π. This ambiguity can be resolved by performing a calculation for the third structure, which represents an intermediate state between (0) and (1).

The source code of `BerryPI` can be downloaded from the GitHub repository. The execution of `BerryPI` requires `WIEN2k` [87] and `WIEN2WANNIER` [88] installed along with `Python` and the `NumPy` library.

Table 3.1: Calculation flow

Command	Description	Input files	Output files	Package
`x kgen -fbz`	Generates a k-mesh in the full Brillouin zone	kgen.def case.struct	case.outputkgen case.klist case.kgen	WIEN2k
`write_w2win case`	Prepare the input for w2w with the occupied band range[a]	case.struct case.outputkgen	case.w2win	WIEN2WANNIER
`write_win case`	Create the input file for w2w	case.struct case.outputkgen case.klist case.w2win	case.win	WIEN2WANNIER
`win2nnkp.py case`	Generate the nearest neighbor list of k-points	case.win	case.nnkp	BerryPI
`write_w2wdef case`	Create definition file for w2w	—	w2w.def	WIEN2WANNIER
`x lapw1 (-c)`	Calculate wave functions for the new k-list	case.struct case.klist	case.vector case.energy	WIEN2k
`w2w case`	Calculate the overlap matrix $\mathbb{S}_{mn}(\mathbf{k}_j, \mathbf{k}_{j+1})$	case.struct case.nnkp case.vector case.energy case.vsp case.w2win case.dayfile	case.mmn	WIEN2WANNIER
`mmn2pathphase.py case x`	Calculate the Berry phase along x-axis [b]	case.mmn case.win	case-x.pathphase	BerryPI

[a] The range of bands from 1 to the last occupied band is taken from `case.scf` file

[b] `x`, `y` or `z` are used to specify the Cartesian axes along which the Berry phase is calculated

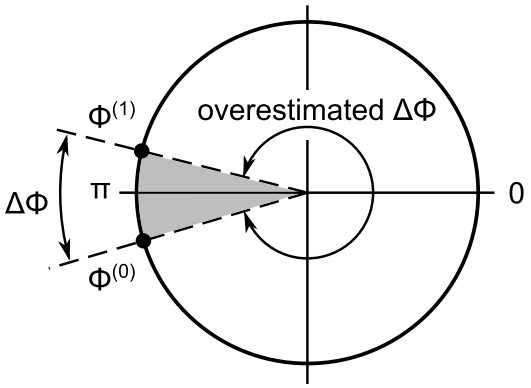

Figure 3.3: Phase map that illustrates two ways of computing the phase difference $\Delta\Phi$.

3.6 Validation

First, we begin with calculation of polarization in the case where the outcome can be predicted exactly. For non-interacting (noble) atoms the net polarization is zero. Therefore the electronic and ionic polarization should cancel each other $P_{\text{ion}} + P_{\text{el}} = 0$. This property is used in order to test the accuracy of our calculations of polarization.

Two helium atoms were placed in a tetragonal cell as illustrated in Fig. 3.4. The cell dimensions $a = 10$ and $b = c = 5$ Bohr were chosen in order to prevent a possible interaction between neighboring atoms. The reference structure had one atom positioned in the origin, while the second atom was placed at $\rho_x = 0.5$, $\rho_y = \rho_z = 0$. In the perturbed structure, the second atom was slightly displaced in the x direction.

The standard self-consistency LAPW cycle was executed with `WIEN2k` for both structures using one k-point. It is strongly advised *not* to use an iterative diagonalization option in the self-consistency cycle prior to the Berry calculation, as it will

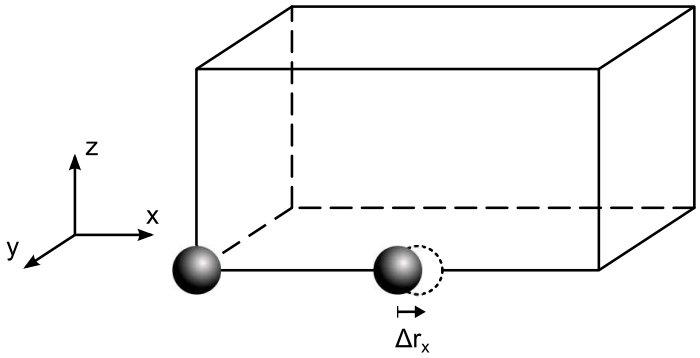

Figure 3.4: The unit cell containing two noble atoms used for the test. One of the atoms is displaced from its centrosymmetric position.

likely lead to spurious results. We forced `WIEN2k` to preserve the symmetry of a perturbed structure when performing the calculation for the reference (centrosymmetric) case. Then we calculate the electronic and ionic polarization for both structures following the steps described in Table 3.1 using a $10 \times 1 \times 1$ k-mesh. The fine mesh in the x direction is required for accurate computation of the Berry phase in Eq. (3.15).

Results of the calculated difference in polarization between the reference and perturbed structures are presented in Table 3.2. It is apparent that the ionic and electronic polarization cancel each other with high accuracy even for very small perturbations. The same calculations were repeated for neon in order to verify the performance in the case of multiple bands and core electrons. The results for the ionic and electronic polarization (Table 3.2) are also consistent with the expectation of zero net polarization, which validates our approach. The sign alternation between the ionic and electronic components of polarization is due to 2π wrapping applied to the phase.

Table 3.2: Test for noble atoms

		Change in the polarization ($\mathrm{C/m^2} \times 10^{-3}$)	
Element	Displacement	ΔP_{ion}	ΔP_{el}
	$0.001a$	4.5802	-4.5814
He	$0.002a$	9.1604	-9.1604
	$0.005a$	22.8966	-22.9058
Ne	$0.001a$	-18.3210	18.3234
	$0.05a$	-916.0496	916.0496

3.7 Applications

In the following, we provide two examples on calculation of the material properties related to polarization using `BerryPI`. The examples include modeling the spontaneous polarization of perovskite crystals and calculation of the Born effective charge of polar materials.

3.7.1 Spontaneous polarization

Spontaneous polarization P_s is one of the major characteristics for ferroelectric materials. It is defined as the change in polarization that occurs when the crystal undergoes a phase change from the centrosymmetric structure to a structure without an inversion symmetry

$$P_{\mathrm{s}} = P_{\mathrm{nc}} - P_{\mathrm{c}} \ . \tag{3.17}$$

Here P_{nc} and P_{c} refer to the polarization values for non-centrosymmetric and centrosymmetric structures, respectively. Figure 3.5 illustrates a particular example of

the ABO_3 perovskite crystal in two different phases: cubic (centrosymmetric) and tetragonal (non-centrosymmetric).

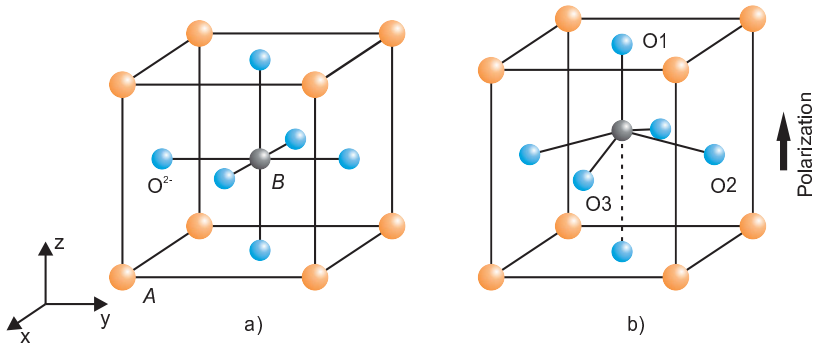

Figure 3.5: Perovskite ABO_3 cubic (a) and tetragonal (b) crystal structures.

For our study we selected some of the most well characterized perovskite compounds: $BaTiO_3$, $KNbO_3$ and $PbTiO_3$. The calculations were performed with the `WIEN2k` package using the generalized gradient approximation [94] (GGA) for the exchange correlation functional and $6 \times 6 \times 6$ sampling of the Brillouin zone. The radii R_{MT} of muffin tin spheres centered around individual atoms are chosen to be equal 2.5, 2.5, 2.26, 1.77, 1.7 and 1.5 Bohr for Ba, K, Pb, Nb, Ti and O, respectively. The product of the minimum R_{MT} radius and the maximum cut-off wave vector in the reciprocal space was kept at a constant value of $R_{\mathrm{MT}}K_{\mathrm{max}} = 7$ throughout all calculations. The energy to separate core and valence electrons was set such that electrons in the following orbitals were treated as valence electrons: Ba – $5s$ $5p$ $6s$, K – $3s$ $3p$ $4s$, Pb – $4f$ $5d$ $6s$ $6p$, Nb – $4s$ $4p$ $4d$ $5s$, Ti – $3s$ $3p$ $3d$ $4s$ and O – $2s$ $2p$. In order to minimize the discrepancy between experimental and theoretical structures, we adopted the experimental values [95–97] of the lattice constant for all three compounds in our calculations. The internal degrees of freedom for tetragonal ferroelectrically distorted

structures were fully relaxed by minimizing the Hellmann-Feynman forces acting on atoms below 0.2 mRy/Bohr. For the cubic centrosymmetric structures, the atomic positions and structural parameters were adjusted accordingly by keeping system volume same as in the tetragonal ferroelectric state. The convergence tests performed with a denser k-mesh $10 \times 10 \times 10$ and $R_{\mathrm{MT}}K_{\max} = 8$ indicate that the polarization calculation itself is not sensitive to these parameters (only 0.3% difference). However, a special care should be taken to obtain accurate atomic positions. This is why the force convergence criteria is reduced down to 0.2 mRy/Bohr, which is less than the default value by a factor of 10.

Results of our calculations of the spontaneous polarization in $BaTiO_3$, $KNbO_3$ and $PbTiO_3$ compounds are summarized in Table 3.3. Our results are consistent with the experimental data and results of other first-principle calculations. Next we explore the sensitivity of calculation results to the choice of the basis set (LAPW vs. plane waves). The same calculations were repeated with the `ABINIT` package [85] using Hartwigsen-Goedecker-Hutter pseudopotentials with semicore electrons for K, Ti, Nb and Ba [98]. Due to the presence of semicore electrons, the cutoff energy was chosen to be relatively high (30 Ha). In this calculation the k-mesh, lattice parameters and atomic positions were kept identical to those used in `WIEN2k`. Our `ABINIT` results (Table 3.3) are in agreement with LAPW (`BerryPI`) data within 10% accuracy range.

3.7.2 Born effective charge

The Born effective charge reveals the mixed ionic and covalent character of bonds and provides further insight into understanding the origin of polarization effects in

Table 3.3: Spontaneous polarization (C/m^2) for perovskite compounds.

Compound	BerryPI	ABINIT	Experimental	Other calculations[1]
$BaTiO_3$	0.31	0.28	0.26 [102]	0.22 [99], 0.29 [100]
$KNbO_3$	0.36	0.34	0.37 [103]	0.3 [101]
$PbTiO_3$	0.86	0.84	0.75 [104]	0.88 [83]

solids [105]. By definition, the Born effective charge of an atom in a solid is related to the change in polarization due to the displacement of this atom from its equilibrium position [106]

$$Z^*_{s,\alpha\beta} = \frac{\Omega}{e} \frac{\partial P_\alpha}{\partial r_{s,\beta}} \ . \tag{3.18}$$

It is convenient to express the effective charge in terms of the total phase using Eq. (3.11), which yields

$$Z^*_{s,\alpha\beta} = (2\pi)^{-1} \frac{\partial \Phi_\alpha}{\partial \rho_{s,\beta}} \ . \tag{3.19}$$

The zz component of the Born effective charge tensor was calculated for tetragonal $BaTiO_3$ and $PbTiO_3$ structures using the same parameters as described in Sec. 3.7.1. Individual atoms were displaced by $\rho_{s,z} = \pm 0.01$, while keeping the position of other atoms unchanged. The self-consistent electron density was obtained for each perturbation. The corresponding change of the total phase along the z axis was used in order to compute the derivative in Eq. (3.19). The calculated Born effective charges

[1] [99]: Projector augmented waves, with the local density approximation (LDA) for the exchange-correlation functional.

[100]: Projector augmented waves, LDA

[101]: LAPW (linear response), LDA

[83]: LAPW-GGA

are presented in Table 3.4. The results obey the acoustic sum rule $\sum_s Z^*_{s,\alpha\beta} = 0$ with a negligible error. We also report calculation of the effective charge for binary zinc-blende (GaAs) and rock-salt (NaCl) structures. Our data are also consistent with results of other first-principle calculations listed in Table 3.4.

Table 3.4: Born effective charge Z^*_{zz} in units of elementary charge for tetragonal perovskite crystals

Compound	Atom	BerryPI	Other calculations
	Ba	+2.77	+2.83 [105]
	Ti	+5.90	+5.81 [105]
$BaTiO_3$	O1	−4.79	−4.73 [105]
	O2	−1.97	−1.95 [105]
	O3	−1.97	−1.95 [105]
	Pb	+3.50	+3.52 [83]
	Ti	+5.34	+5.18 [83]
$PbTiO_3$	O1	−4.51	−4.38 [83]
	O2	−2.14	−2.16 [83]
	O3	−2.14	−2.16 [83]
GaAs	As	−2.21	−2.00 [107]
NaCl	Na	+1.11	+0.99 [108]

Chapter 4

Ferroelectric switching with domain wall motion

We want to put a note that several contents of the current chapter appear in an article under review [S.J. Ahmed, S. Pichardo, L.Curiel, O.Rubel, "First-principle modelling of the ferroelectric switching in $BaTiO_3$: concurrent switching vs domain wall motion"].

4.1 Introduction

The introduction of `BerryPI` to the selected tool `WIEN2k` enables the computation polarization based properties of the ferroelectric material which allows us to focus on our goal of reducing the excess heat generated in ferroelectric materials. As discussed in chapter 1, the performance of a ferroelectric systems is governed by switching of polarization due to an external electric field. The switching occurs via nucleation of domains with inverse polarization followed by their growth. The latter is referred to

as domain wall motion. The domain wall motion is considered to be responsible for hysteresis energy loss in ferroelectrics, which is the sources of excess heat generated in ferroelectric materials during operation [17, 33].

Domain walls in ferroelectric materials have been studied theoretically mostly using semi-empirical molecular dynamics [47, 109–113]. Shin et al. [112] proposed the most well established theory of the nucleation and motion of domain wall using molecular dynamics simulation. Their study emphasized that it is always easier to create a two-dimensional nucleus at the domain interface compared to creating a three-dimensional nucleus in uniform bulk material, as the latter introduced larger domain wall areas which results in larger energy penalty. The model wass able to capture both the nucleation of domains and their successive growth in response to the applied electric field. However, this approach relies on inputs from first principle studies [49, 50], such as the interatomic potential, domain wall formation energy, spontaneous polarization and its profile across the wall.

Nevertheless, quantum mechanical *ab initio* investigations of domain walls in ferroelectrics are mostly limited to calculation of their formation energy [49, 114]. Meyer and Vanderbilt [50], Beckman et al. [115] further advanced the first-principle modeling of propagation of domain walls and determined the energy barrier associated with the motion of 180° and 90° walls in $PbTiO_3$. Results of their study are applicable to the growth of established domains, whereas the initial (nucleation) phase and most importantly the associated energy barrier remains overlooked. This gap motivated us to perform a full polarization reversal study considering both the domain nucleation and propagation stages using first-principles.

4.2 Landau theory

Landau theory was proposed in the context of order disorder transformation in superconductors and ferroelectric systems that involves a change in the symmetry [116, 117]. The theory enables calculation of symmetry based properties with a minimal number of input parameters from either experimental or microscopic calculations and thereby, is considered as a bridge between macroscopic observation and microscopic models. Landau theory is capable of describing the equilibrium behavior of the system near the phase transition. However, the transition between phases with a change of symmetry does not take place smoothly. The thermodynamic state of the two symmetrically distinct phases must be identical at the transition point. The transition between phases is characterized by an internal variable of the system called the order parameter. The parameter has a value of zero in the high symmetry or unperturbed phase which changes continuously as the symmetry is lowered by a phase transition [118–120]. To describe the ferroelectric phase transition, the entity polarization serves as the order parameter [121].

4.3 Landau-Devonshire theory

Devonshire's extension to the Landau's symmetry-based consideration provided the description of first and second order phase transitions in a ferroelectric bulk system with spatially uniform polarization [118–120]. Devonshire's explanations were based on fundamental principles of ferroelectrics. The model expresses the thermodynamic state of a system as a function of a specific set of variables or order parameters.

Another important consideration in the model is, in thermal equilibrium, the values of these order parameters or variables minimize the free energy of the system.

The total energy of a system within Landau-Devonshire(LD) theory can be expanded as power series of the order parameter polarization [121, 122].

$$E(P) = a\,P^2 + b\,P^4 + c\,P^6 \tag{4.1}$$

Here, a, b and c are coefficients that describes the phase transition. The value of a varies as a function of temperature, T.

$$a = a_0(T - T_c) \tag{4.2}$$

Here, T_c is the characteristic Curie temperature of the material at which second order transition takes place. The constant b takes a positive value for a process involving a second order transition however, it becomes negative while c becomes positive in case of a first order transition. Since, the scope of the present work is limited to second order transition only, the equations are expressed only in terms of a and b in the following chapters.

Figure 4.1 shows the change in potential energy profile with decreasing/increasing temperatures generated by the LD model. At higher temperature, the energy profile assumes a parabolic shape while a remains positive. As the temperature is lowered to T_c, a phase transition starts to occur where the constant a becomes null. As the temperature is lowered below T_c, the ferroelectric crystal undergoes a second order transition to the ferroelectric phase and the potential profile takes a double well shape by changing the constant a to a negative quantity.

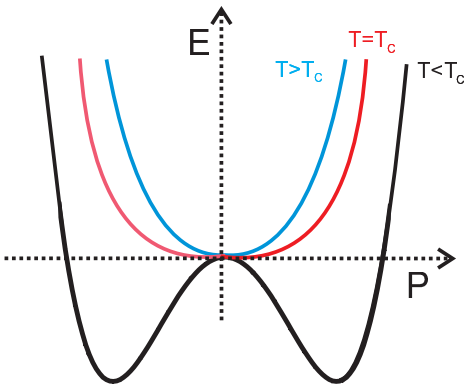

Figure 4.1: Schematic of variation of energy in terms of polarization at different temperatures as the ferroelectric material undergoes a second order phase transition

Application of a constant electric field $\mathcal{E}$ alters the system's total energy as follows [122],

$$E(P) = a\,P^2 + b\,P^4 - \mathcal{E}\,P \tag{4.3}$$

The minima of $E(P)$ in Eq. (4.3) where $\frac{\delta E}{\delta P} = 0$ determines the equilibrium configuration of the system. Mathematical solution yields the expression for electric field as a function of polarization as [121, 122],

$$\mathcal{E}(P) = 2\,a\,P + 4\,b\,P^3 \tag{4.4}$$

Figure 4.2 depicts the LD model generated Eq. (4.4) polarization response of the ferroelectric crystal to the electric field applied at different transition temperatures. At a temperature above T_c, the material is in the paraelectric state characterized by a linear response to applied electric field. As the temperature reaches T_c, a second order transition starts to commence. Below T_c, the material's response to applied electric field takes a hysteresis form when the material has attained a second order phase transition to the ferroelectric phase.

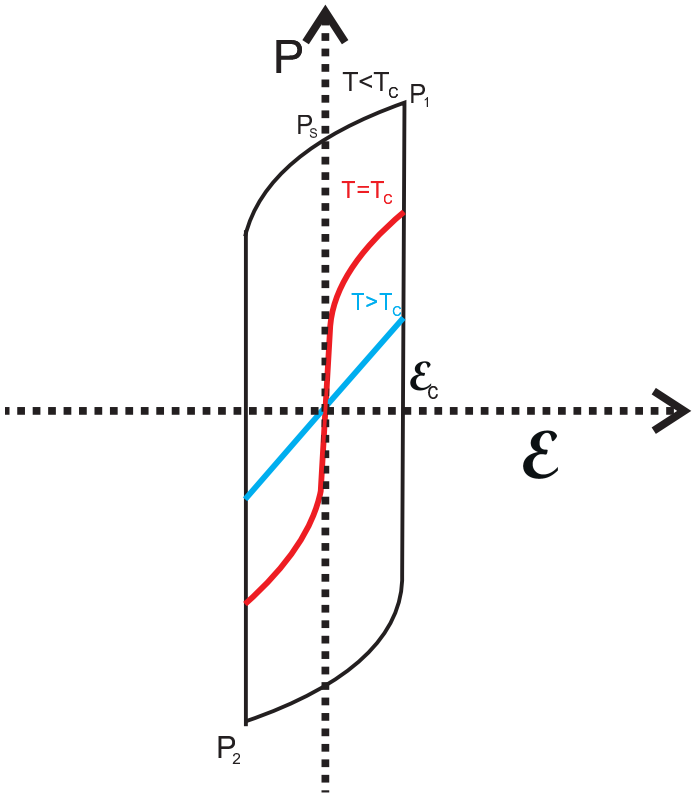

Figure 4.2: The polarization response of a ferroelectric material to the applied electric field $\mathcal{E}$ at different temperatures captured using LD theory

In response to an alternating electric field, when a ferroelectric material switches between alternating states of polarization, the loss during the process can be given by the energy that is not recovered during the process. The loss can be written mathematically as,

$$\begin{aligned} W_{loss} &= \oint P \, d\mathcal{E} \\ &= \int P_{1\,to\,2} \, d\mathcal{E} - \int P_{2\,to\,1} \, d\mathcal{E} \end{aligned} \tag{4.5}$$

which corresponds a switching process where the polarization is switched from state P_1 to state P_2 first and then, switched back to state P_1 in response to the alternating field. As evident from Fig. 4.2, when the ferroelectric switching takes a hysteresis form below T_c, the energy spent to switch the material to an alternating equivalent state, is not recovered during returning back to the initial state as the switching takes a different path. The energy that is not recovered during the process can then be given by the area of the hysteresis loop which corresponds to energy loss during the polarization reversal process. As mentioned in chapter 1, this loss energy due to hysteresis is converted into heat and causes a thermal rise in the material [17, 33].

Figure 4.2 also shows that the major contribution to the ferroelectric loss comes from the coercive field, $\mathcal{E}_c$ which is defined as the field required to balance the polarization between oppositely polarized domains resulting in a vanishing net polarization of the material. Another property on which the energy loss depends, is the spontaneous polarization, P_s of the material. Application of an alternating electric field with a peak amplitude $\mathcal{E}_c$ switches the materials polarization states between P_1 and P_2 according to Eq. (4.3). The spontaneous polarization, P_s depends on the fundamental lattice configuration of the material. However, the coercive field, $\mathcal{E}_c$ depends

mainly on the formation of domain walls between regions of opposite polarization and their relative propagation [33]. The fundamental lattice portion also plays an important role to $\mathcal{E}_c$ as it significantly influences the motion of domain walls which will be addressed in the later sections of this chapter.

4.4 Domain wall

The existence the multiple states of spontaneous polarization in different crystallographic directions gives rise to the concept of domain wall as in a crystalline material, it is possible for these polarization states to get oriented against each others. A domain is defined as the volume in the material where the spontaneous polarizations in individual elementary cells are oriented in the same direction [123]. Domain walls are defined as the boundary between oppositely polarized domains.

The number of possible domain states and domain wall configurations are a dependant on the number of possible spontaneous polarizations states. For tetragonal perovskites, six possible orientations of spontaneous polarization perpendicular to each other are possible. This results in two possible sates (Fig. 4.3) of domain wall in these material. One of them presents a situation when the spontaneous polarizations in individual elementary cells are oriented against each other (Fig. 4.3(a)) and is defined as 180^0 domain wall. Another possible configuration conveys 90^0 domain wall when the spontaneous polarizations are oriented perpendicular(90^0)(Fig. 4.3(b)) with respect to each other.

Ferroelectric domain walls are normally considered to be **I**sing type where the polarization switches traversing through a zero polarization along a high symmetry

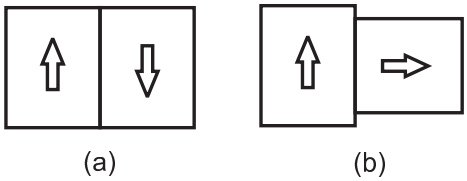

Figure 4.3: Two possible states (a)180^0 (b)90^0 of domain wall in a tetragonal ferroelectric material.

path [124]. **I**sing type switching is regarded favorable in ferroelectric materials because of their strong electrostrictive nature. Polarization reversal through any other path than the high symmetry path would require very high amount of elastic energy [124] due to a large lattice strain. However, several recent studies [125–128] provided the evidence of the **B**loch-like and Néel-like rotation of polarization through a curved path. **B**loch type switching refers to the rotation of polarization in planes parallel to the domain wall and Néel type deals with rotation occurring in planes perpendicular to the domain wall. The study on this curved switching nature is discussed in chapter 5.

In this study, we perform a theoretical study of **I**sing type polarization reversal via 180° domain wall motion in $BaTiO_3$, which is one of the most well characterized perovskite compounds. Calculations of the energy profile suggest that the ferroelectric switching occurs as a result of sequential reversal of polarization in adjacent cells, which is the essence of domain wall formation and motion. The results are applied to calculation of the coercive field for $BaTiO_3$ and compared to a Landau-Devonshire (LD) model [118–120], which is widely used for interpretation of ferroelectric switching phenomenon [129]. We show that both models result in a similar magnitude of the intrinsic coercive field, in spite of the fact that the LD model does not capture effects

associated with the domain wall formation and propagation. This chapter represents several sections of an article submitted for review by the author.

4.5 Computational details

The first-principle calculations are carried out within a linear augmented plane wave method using the density functional theory (DFT) implemented in WIEN2k package [87]. The local spin density approximation [130–132] has been chosen for the exchange correlation functional, since it was successfully applied previously [50, 115, 133] to study ferroelectric materials and their properties. The Brillouin zone for single elementary cell calculations was sampled using $6 \times 6 \times 6$ k-mesh. In the case of supercell calculations, the k-mesh was adjusted accordingly in order to maintain the same k-point density. The radii R_{MT} of muffin tin spheres centered at individual atoms are chosen to be equal 2.3, 1.8 and 1.54 Bohr for Ba, Ti and O, respectively. The product of the minimum R_{MT} radius and the maximum cut-off wave vector in the reciprocal space was kept at the constant value of $R_{\mathrm{MT}} K_{\mathrm{max}} = 7$ throughout all calculations. The energy to separate core and valence electron was set such that electrons in the following orbitals were treated as valence electrons: Ba – $5s$ $5p$ $6s$, Ti – $3s$ $3p$ $3d$ $4s$ and O – $2s$ $2p$.

Self-consistent structural parameters of $BaTiO_3$ were used in the calculations. The internal degrees of freedom for tetragonal structures were fully relaxed by minimizing the Hellmann-Feynman forces acting on atoms below 0.2 mRy/Bohr. The fully optimized structural parameters are listed in Table 4.1.

The polarization inversion in the single cell was associated with a reaction co-

Table 4.1: Structural parameters for $BaTiO_3$ in the tetragonal phase obtained theoretically and experimentally.

Structural parameters	Present calculations	Experimental structure [134]	Other DFT calculations [25]
a (Å)	3.93	3.986	3.929
c/a	1.005	1.01	1.01
$\delta z_{\mathrm{Ba}}/c$ (fixed)	0.0	0.0	0.0
$\delta z_{\mathrm{Ti}}/c$	0.009	0.015	0.009
$\delta z_{\mathrm{O}_1}/c$	-0.015	-0.023	-0.013
$\delta z_{\mathrm{O}_2,\mathrm{O}_3}/c$	-0.01	-0.014	-0.009

ordinate ξ, which takes the values of 1 and 0 for the relaxed ferroelectric tetragonal structure and the corresponding centrosymmetric structure, respectively. The structural parameters for an arbitrary transition state ξ were determined by a linear interpolation

$$\delta z(\xi) = \delta z(1)\,\xi \ . \tag{4.6}$$

We assumed that the tetragonality of the lattice remained unchanged during this transition.

Polarization properties were calculated based on the modern theory of polarization [80, 82] in the framework of Berry phase approach [91]. This capability is implemented in a `BerryPI` package [75] for `WIEN2k` in conjunction with `WIEN2WANNIER` code [88].

4.6 Results and discussion

4.6.1 Ferroelectric switching and domain wall motion

Devonshire's [118–120] extension of the original Landau model to polarization inversion in perovskite crystals implies a concurrent switching of the body-centred atom between two equivalent positions in the entire structure. However, this ansatz is not consistent with the existence of domain walls, which require formation and growth of regions with opposite polarization. In order to identify which of the two scenarios is more favourable, we compare a potential energy profile associated with the polarization inversion in single cell and supercell models.

Figure 4.4 shows a potential energy curve that corresponds to the variation of total energy as function of Ti-atom position for a $BaTiO_3$ single cell. The barrier for switching between two equilibrium positions is found to be $E_b = 2.8$ meV, which represents the concurrent switching. Previous theoretical studies [19, 129] indicate that the barrier height is extremely sensitive to the choice of an exchange correlation functional, mismatch of the lattice parameters and the choice of the basis set, which results in a wide range of values reported $E_b = 5 \ldots 100$ meV. Therefore, we base further discussion on the relative difference in the barrier height rather than its absolute value.

In order to model the ferroelectric switching via a domain wall motion, we choose a supercell that consists of six unit cells as illustrated in Fig. 4.5(a). It was previously shown [50] that such a supercell is large enough to capture the 180° domain wall energy accurately. According to our hypothesis, the ferroelectric switching occurs via consecutive switching of polarization in adjacent unit cells as depicted in Fig. 4.5(a-c),

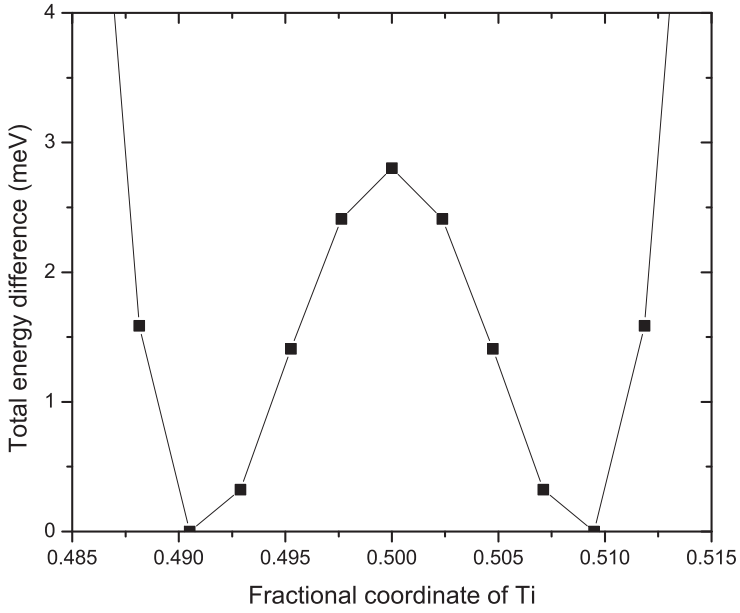

Figure 4.4: Potential profile associated with polarization inversion for a single unit cell of $BaTiO_3$ in the absence of an external electric field. (Lines are a guide to the eye)

which represent the nucleation and growth of the domain with opposite polarization. Additional constraints were applied to Ba and Ti atoms in the cells directly adjacent to the switching cells in order to prevent the structure from formation of a single domain. However, the forces acting on those atoms did not exceed 3 mRy/Bohr. The corresponding potential profile is presented in Fig. 4.5(e) (solid line).

In contrast to the single cell switching, the potential profile for consecutive process is non-monotonic with a series of peaks associated with the barriers to be overcome during switching of individual cells. The energy barrier for the nucleation stage (Fig. 4.5(a)) is about 2-3 times higher than the barriers corresponding to the propagation phase. The latter are notably lower than the barrier for concurrent switching (Fig. 4.5(d)). Moreover, the barrier height reduces significantly as the size of domain with opposite polarization grows. The resultant barrier for consecutive switching of polarization in the entire supercell is approximately 8 meV, which is half that compared to the concurrent process (Fig. 4.5(e) solid vs. dashed line, respectively). This result favors the existence of domain walls and their propagation as a mechanism for ferroelectric switching.

4.6.2 Coercive field

In this section, we apply results of the domain wall motion study to calculate the intrinsic coercive field of $BaTiO_3$. It is known from previous studies [115, 135] that theoretical models largely overestimate (by orders of magnitude) the coercive fields observed experimentally. The lower coercive field measured experimentally are traditionally attributed to extrinsic factors [135], such as the defect-mediated nucleation of

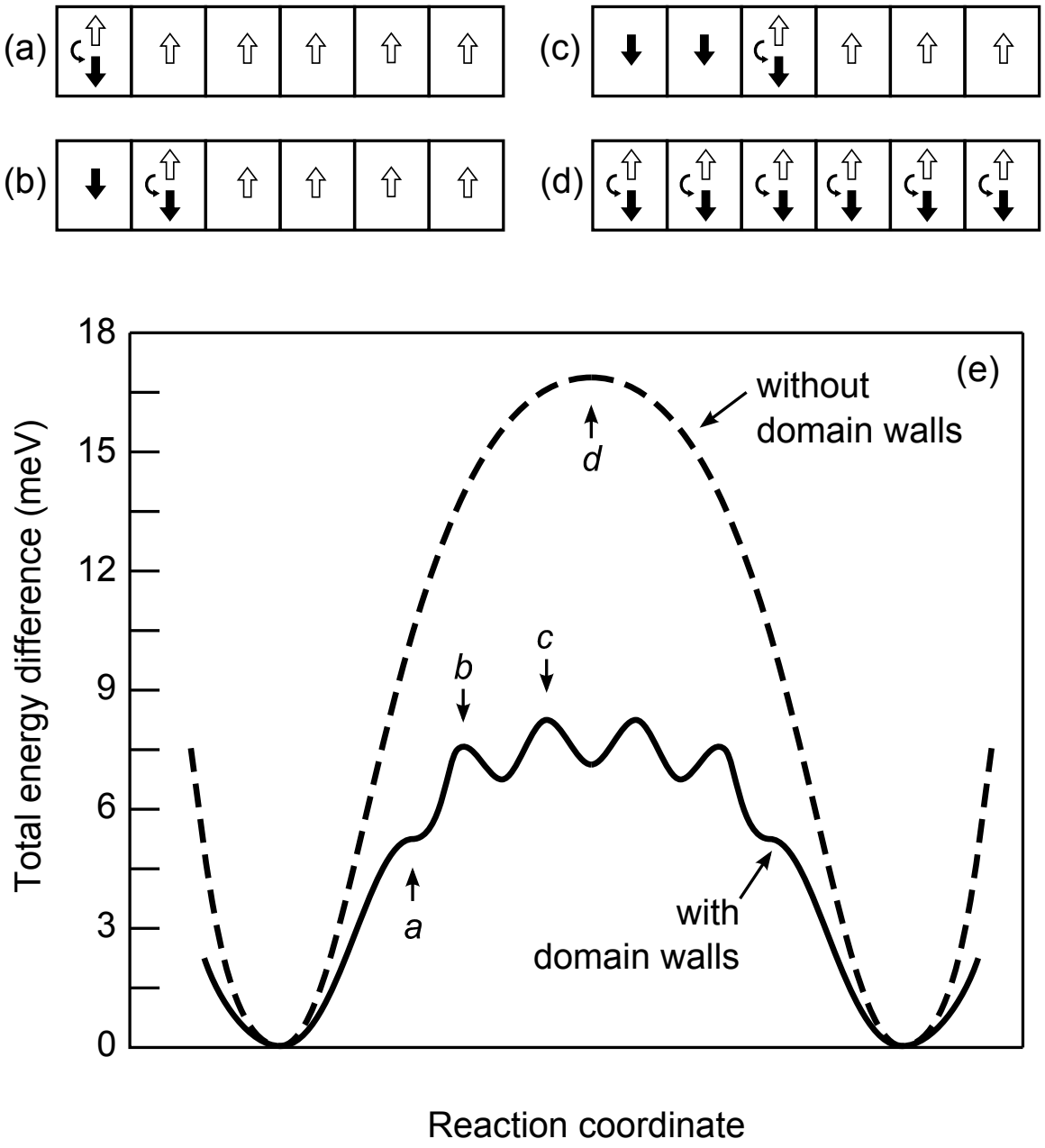

Figure 4.5: Consecutive (a-c) and concurrent (d) processes of polarization inversion in $BaTiO_3$ supercell. The arrows on panels (a-d) illustrate the polarization vector of individual unit cells. The total energy variation during the switching process is shown on panel (e) as a function of the reaction coordinate for both scenarios. The energy barriers are linked with the corresponding structural transitions (a-d).

domains [133, 136], which is not captured in the ideal structures studied theoretically. The physical coercive field is often identified as the field at which the domain walls become unpinned [115](i.e, mobile).

According to the definition of the electric enthalpy, the electric field corresponds to a slope of the total energy density U vs polarization curve [115]. The coercive field is then determined by the maximum slope of $U(P)$ function along the reaction (switching) path

$$\mathcal{E}_{\mathrm{c}} = \left.\frac{dU}{dP}\right|_{\mathrm{max}} . \tag{4.7}$$

Figure 4.6 represents the energy profile as a function of polarization for two distinct mechanisms of ferroelectric switching. Using this energy profile we estimate the coercive field of 68 MV/m for $BaTiO_3$ considering only the propagation phase, which represents the domain wall unpinning.

Next, it will be instructive to compare our result for the coercive field with other methods based on the single-domain switching. The potential energy profile as a function of polarization for single unit cell can also be readily obtained from DFT calculations (Fig 4.7). The same energy density profile can also be expressed in terms of the LD model using the power series [122]

$$U(P) = \frac{E_{\mathrm{b}}}{\Omega_0}\left[2(P/P_{\mathrm{s}})^2 - (P/P_{\mathrm{s}})^4\right] , \tag{4.8}$$

where E_{b} is the energy barrier height, Ω_0 is the equilibrium unit cell volume and P_{s} is the spontaneous polarization. As evident from Fig. 4.7, the LD model matches the DFT energy profile. The coercive field can be expressed analytically in terms of LD model parameters as [115]

$$\mathcal{E}_{\mathrm{c}} = (4/3)^{3/2}\frac{E_{\mathrm{b}}}{\Omega_0 P_{\mathrm{s}}} . \tag{4.9}$$

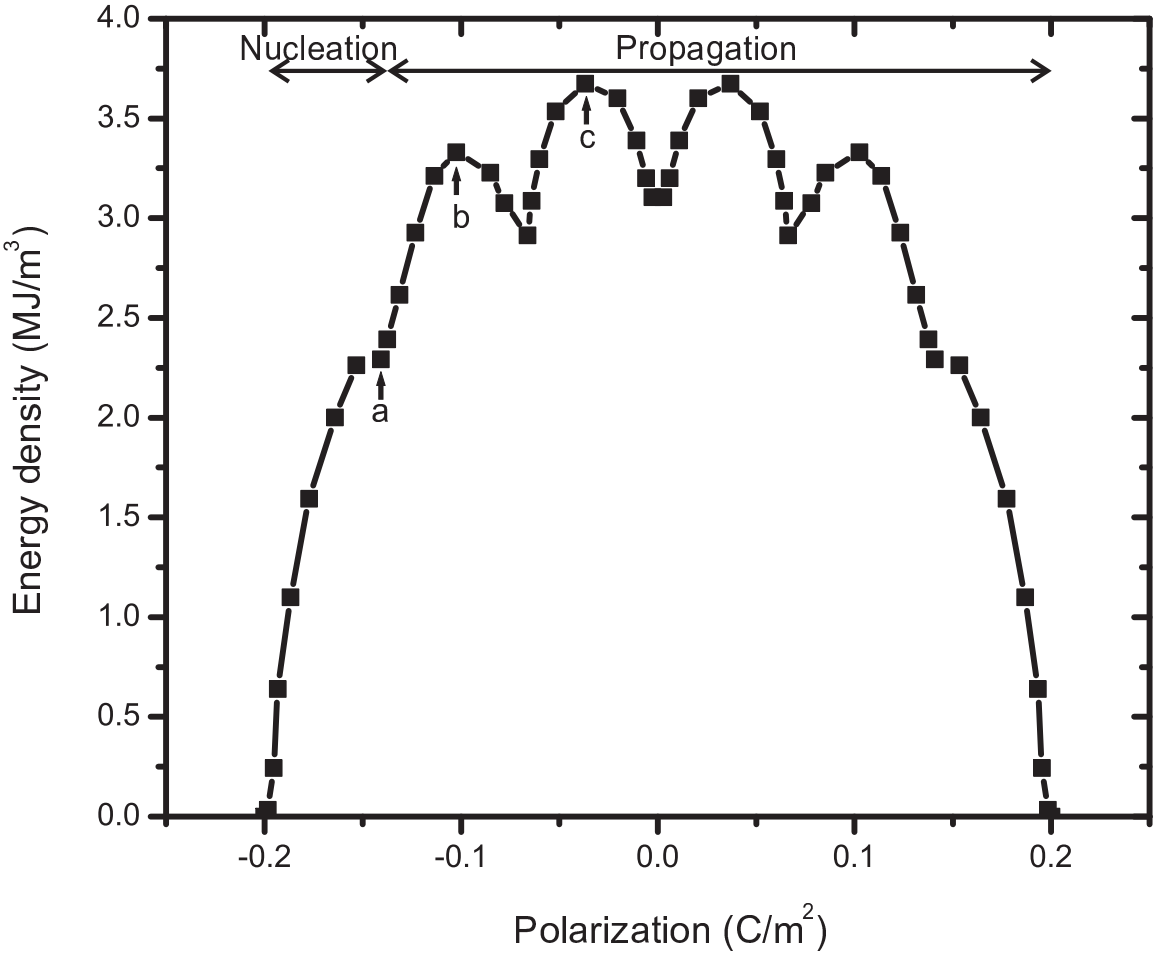

Figure 4.6: Energy profile as a function of polarization considering nucleation and propagation of domain walls. The labels *a-c* refer to the barriers for consecutive switching of individual cells shown in Fig. 4.5(a-c).

Equation (4.9) yields the coercive field of $\mathcal{E}_c = 57$ MV/m for the potential curve shown in Fig. 4.7. This result is remarkably close to that obtained for the propagation phase of the domain wall motion ($\mathcal{E}_c = 68$ MV/m). The limited width of the domain wall implied in our study can explain the similarity between the coercive field results obtained with and without domain walls [137].

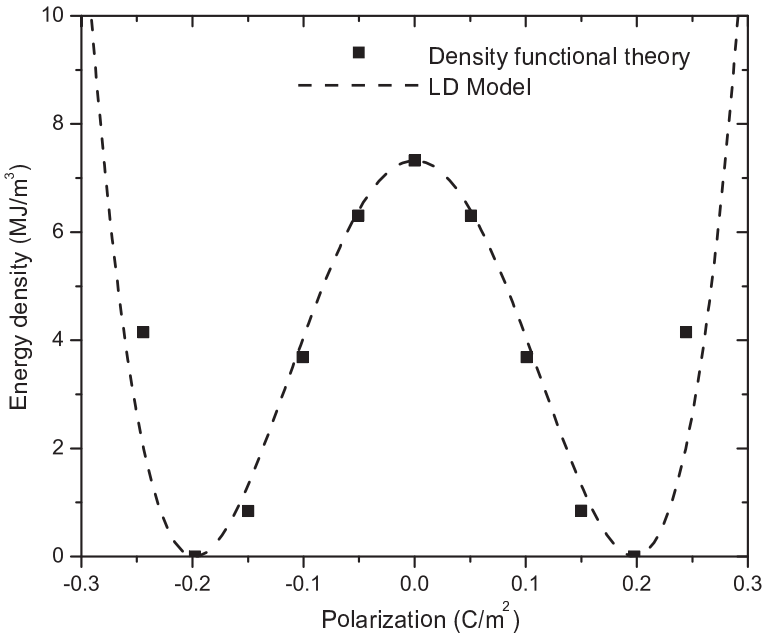

Figure 4.7: Total energy evolution as a function of polarization corresponding to a single-domain ferroelectric switching. Results are calculated using DFT and fitted to LD model Eq. (4.8) with the following parameters: $E_b = 2.8$ meV, $\Omega_0 = 61.2$ Å^3 and $P_s = 0.20$ C/m^2.

Finally, it should also be noted that the values of the coercive field calculated here are still much greater than the experimental results of $\mathcal{E}_c \sim 0.07$ MV/m for $BaTiO_3$ [138, 139]. Experimentally, the domain wall width for $BaTiO_3$ was found to

be 50 $\mathring{A}$ due to contribution from the extrinsic factors like presence of defects and impurities [140]. However, the polarization profile of the ideal $BaTiO_3$ structure in the current study suggests a domain wall width of nearly one unit cell. Other DFT calculations of domain wall study also found the domain wall width within one unit cell range [49, 114]. Kim et el. [137] showed that the coercive field is strongly dependant on the width of domain wall. The higher domain wall width in experiment due to extrinsic factors explains the reason for observing a lower coercive field experimentally. Study of defect related extrinsic contributions within first principle framework requires a structure that contains large numbers of unit cells which is computationally expensive. In the present work, we establish a basis for domain wall motion study in an ideal structure.

Chapter 5

Ideal ferroelectric switching model

5.1 Introduction

First-principles study of ferroelectric switching between polarization states is mostly based at the Landau Devonshire (LD) model [19, 49, 82]. The model implies that the ferroelectric switching occurs by an **I**sing type polarization rotation in a straight line path achieved by overcoming the energy barrier between the ferroelectric state and cubic paraelectric state in a two dimensional space.

Recently, several studies [124, 126–128] indicated that the ferroelectric switching can also take place by **B**loch-like and N*é*el-like polarization rotation through an optimum curved path. Because of this curved nature of the path, switching may also be guided in a manner that the polarization reversal process needs much lower energy barrier to be overcome.

Here, in order to validate previous studies, we first make attempts to determine the curved nature of the optimum switching path. We choose to perform a first-

principle potential energy profile study on a three dimensional surface among four equivalent polarization states that are oriented in different directions within [010] plane. The energy surface study is carried out on $PbTiO_3$ which is one of the most well characterized material. We confirm that the ferroelectric switching takes place in a curved path with much lower energy barrier than the **I**sing like switching process. As a result, the intrinsic coercive field required for polarization reversal is also much lower than the field predicted by ferroelectric-paraelectric barrier. Based on the findings, we propose an alternative approach to drive a ferroelectric crystal with the electric field applied in two crystallographic directions that can ensure a much lower hysteresis loss and thus, reduce dielectric dissipation in the material.

5.2 Computational details

The first-principle calculations are performed using the identical computational packages, exchange correlation functional and computation parameters mentioned in section 4.5. The radii R_{MT} of muffin tin spheres centered at individual atoms are chosen to be equal 2.26, 1.68 and 1.49 Bohr for Pb, Ti and O, respectively. The chosen energy to separate core and valence electron treated electrons in the following orbital as valence electrons: Pb – $4f$ $5p$ $5d$ $6s$ $6p$, Ti – $3s$ $3p$ $3d$ $4s$ and O – $2s$ $2p$. The fully optimized structural parameters for $PbTiO_3$ are listed in Table 5.1

Table 5.1: Structural parameters for $PbTiO_3$ in the tetragonal phase obtained theoretically and experimentally.

Structural parameters	Present calculations	Experimental structure [95]	Other DFT calculations [25]
a (Å)	3.858	3.905	3.905
c/a	1.047	1.063	1.063
$\delta z_{\mathrm{Pb}}/c$ (fixed)	0.0	0.0	0.0
$\delta z_{\mathrm{Ti}}/c$	0.033	0.04	0.048
$\delta z_{\mathrm{O_1}}/c$	0.09	0.112	0.120
$\delta z_{\mathrm{O_2,O_3}}/c$	0.102	0.112	0.128

5.3 Potential energy surface

The reaction space for energy surface calculation is chosen between four equivalent polarization states oriented in different directions within [010] plane (Fig. 5.1). The reaction coordinate ξ however, takes values between (1,0), (0,1) and (0,0) for the ferroelectric structures with polarized down state (P_z), polarized left state (P_x) and the corresponding centrosymmetric structure only, as indicated by the shaded region in Fig. 5.1. The energy profile for the full reaction space can be obtained by performing a fourfold symmetry operation on the chosen reaction area where computation of energy and polarization is performed. The structural parameters for an arbitrary transition state ξ is determined by a similar linear interpolation mentioned in Eq. (4.5).

The obtained energy surface takes a hat profile shape as a function of polarization (Fig. 5.2). The profile finds the highest energy barrier for switching between the

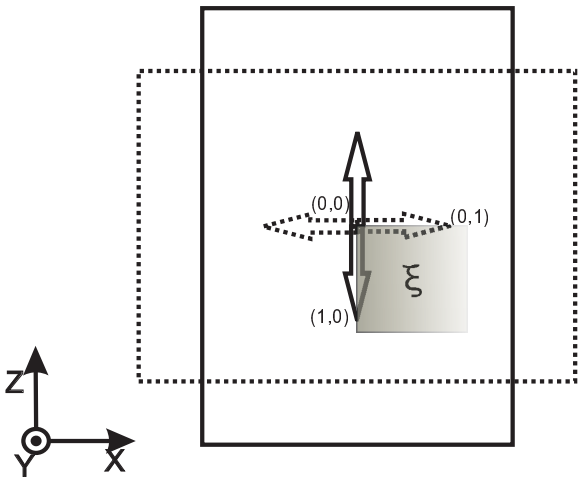

Figure 5.1: Reaction space for building the energy surface. The computation was performed on the shaded area only because of the presence of the fourfold symmetry.

ferroelectric and cubic perovskite phase to be 72 meV. Previous theoretical studies [19, 129] indicate that this barrier height is extremely sensitive to the choice of an exchange correlation functionals, mismatch of the lattice parameters and the choice of the basis sets. The highest energy barrier between ferroelectric and cubic state ranged from 30-600 meV in those studies [19, 129]. Therefore, we also base our discussion on the relative difference in the barrier height rather than its absolute value. The obtained potential energy surface depicts that there exists regions where the corresponding energy barriers are significantly smaller. These regions can be a favorable option for ferroelectric switching path (indicated by arrows in Fig. 5.2). In addition, it may also be possible to guide the switching in a path that the polarization reversal process traverses through these minimum energy barrier regions.

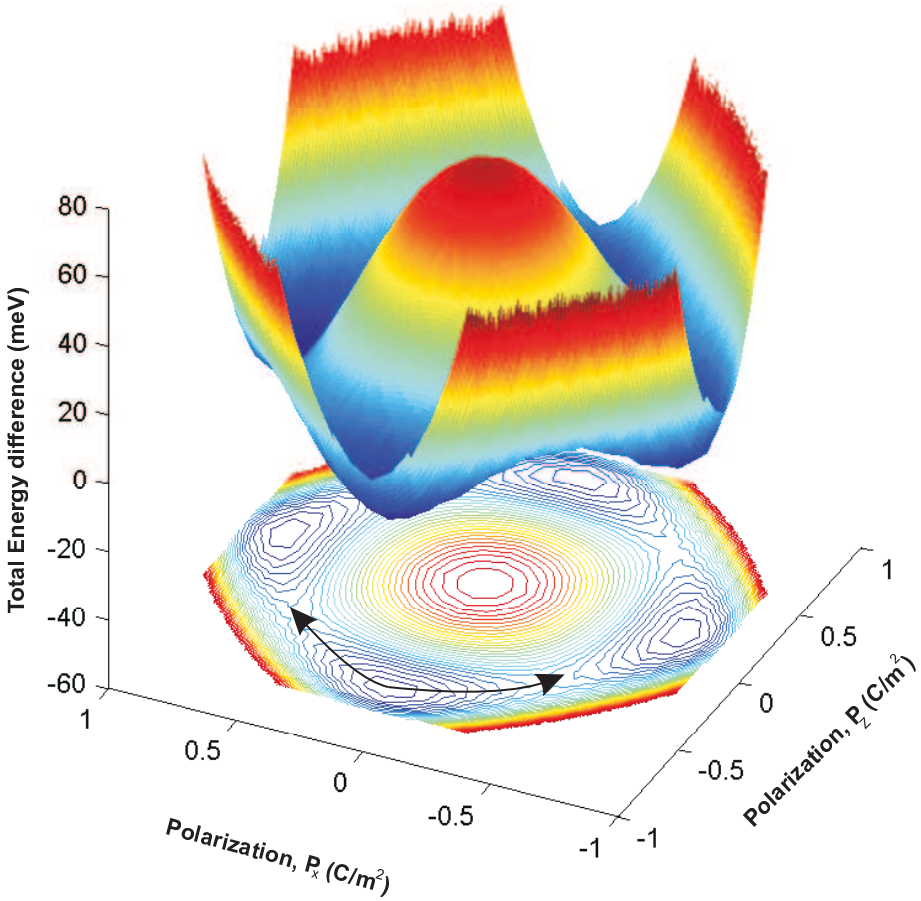

Figure 5.2: The 3-dimensional energy surface obtained from the Reaction space shown in Fig. 5.1. The plot in the bottom represents the contour of the energy surface with the four corner circles denoting the spontaneous polarization states. The maximum in the middle of the contour plot corresponds to the centrosymmetric paraelectric state.

5.4 Optimum switching path

Polarization switching in a ferroelectric is characterized mainly by the coercive field, $\mathcal{E}_C$ of the material which is defined as the field needed to switch polarization between oppositely polarized states. In the framework of conventional theory based on LD model [118–120] which considers an **I**sing like switching, the coercive field is determined by the highest derivative of the energy density profile as a function of polarization. According to Eq. (5.1), the energy density profile in LD theory depends on two parameters: energy barrier for ferroelectric to cubic paraelectric transition and the spontaneous polarization of the crystal [122].

$$U_0(P) = \frac{E_\mathrm{b}}{\Omega_0}\left[2(P/P_\mathrm{s})^2 - (P/P_\mathrm{s})^4\right] \ , \tag{5.1}$$

Where E_b is the energy barrier height, Ω_0 is the equilibrium unit cell volume and P_s is the spontaneous polarization. For $PbTiO_3$, with an energy barrier of 72 meV and a spontaneous polarization of 0.8 C/m^2, the coercive field yields a value of 372 MV/m from the highest derivative of Eq. (5.1). LD theory implies that an alternating electric field with a peak amplitude equivalent to the coercive field obtained from LD model lowers the barrier and switches the material to a polarization state in the field direction and thus switching occurs along straight line path between two ferroelectric states that traverses through the zero polarization cubic paraelectric transition state (**I**sing type).

However, the potential energy surface in Fig. 5.2 depicts regions with much smaller energy barriers that can favor ferroelectric switching. Such regions implies the presence of a smaller derivative of energy density with respect to polarization. Here, we perform an optimum switching path determination study by applying alternative

electric fields to the potential energy surface and observing the evolution of the energy surface as a function of period.

The energy density will change in the following way due to the applied electric field [122],

$$U = U_0 - \mathcal{E}\mathbf{P} \tag{5.2}$$

where U is the energy density in response to an electric field, $\mathcal{E}$. U_0 represents the ground state energy density.

To determine the switching path, we use an algorithm program. The program searches for the optimum path by finding the steepest decent during potential surface tilting by an electric field.

First, we apply an alternating electric field that has a peak amplitude of the coercive field incurred from the LD theory to the potential energy profile along the Z direction. The contour plot of evolution of the energy surface in response to the alternating electric field is shown in Fig. 5.3(b-i) where Fig. 5.3(b) represents the ground state energy surface where all four states of polarization are equally favorable. Figure 5.3(f) corresponds to the $\mathcal{E}_C$= 372 MV/m computed from the LD model which shows that the material has switched to the ferroelectric state in the field direction. However, our path determination program demonstrates that the switching doesn't take place in a linear path through the paraelectric state but rather the process occurs along a curved path as indicated by the arrow in Fig. 5.3(f). It is also worth noticing that the ferroelectric switching along a curved path also takes place (Fig. 5.3(e)) at an electric field of 340 MV/m which is lower than the computed coercive field based

on LD model. However, the next lowest electric field (263 MV/m) of the time period does not favor ferroelectric switching (Fig. 5.3(d)) as the path algorithm suggests that the polarization is situating at an intermediate state of switching. As a result, it can be concluded that the optimum field for polarization reversal lies in between 263 MV/m and 340 MV/m.

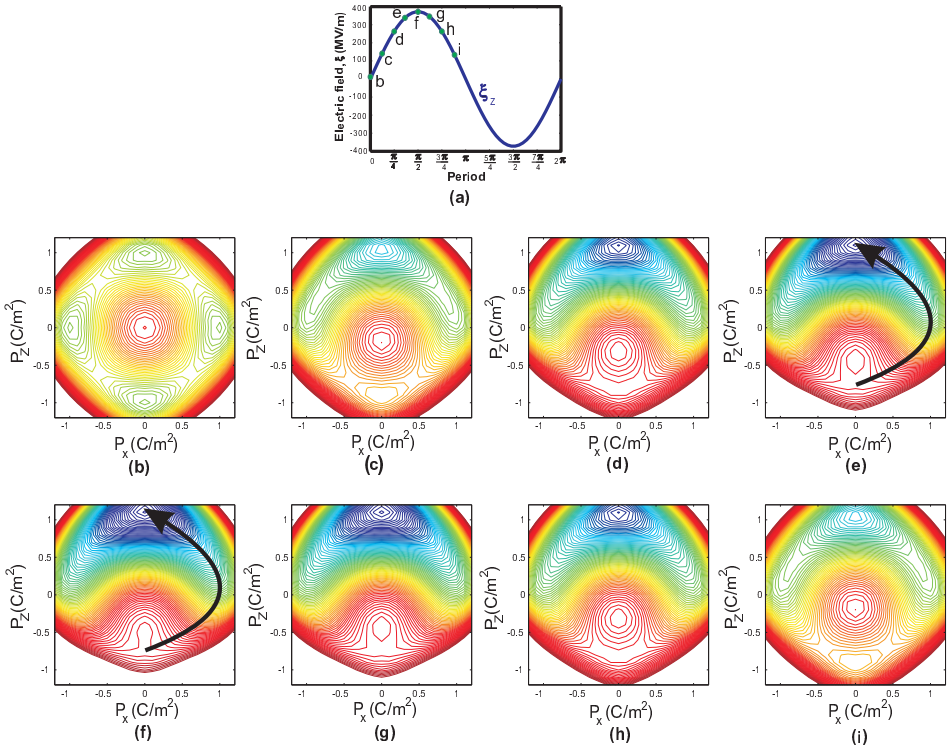

Figure 5.3: The applied alternating electric field (a) has peak value of $\mathcal{E}$= 372 MV/m incurred from LD model. The dots on panels (b-i) are spaced within $\frac{\pi}{8}$ intervals of the time period. Change in potential energy surface at electric fields during those intervals are illustrated on labels (b-i)

Next, we make attempts to determine optimum field required to switch between ferroelectric states by applying several magnitudes of alternating electric field ranging from 263 MV/m to 340 MV/m. We find the field at which ferroelectric switching

takes place (coercive field) to be 325 MV/m. Figure 5.4(b-i) shows the development of potential energy surface in response to an alternating field having a peak amplitude equivalent to the optimum field. Figure 5.4(f) corresponds to the energy surface at the coercive field where the switching takes place in a curved path.

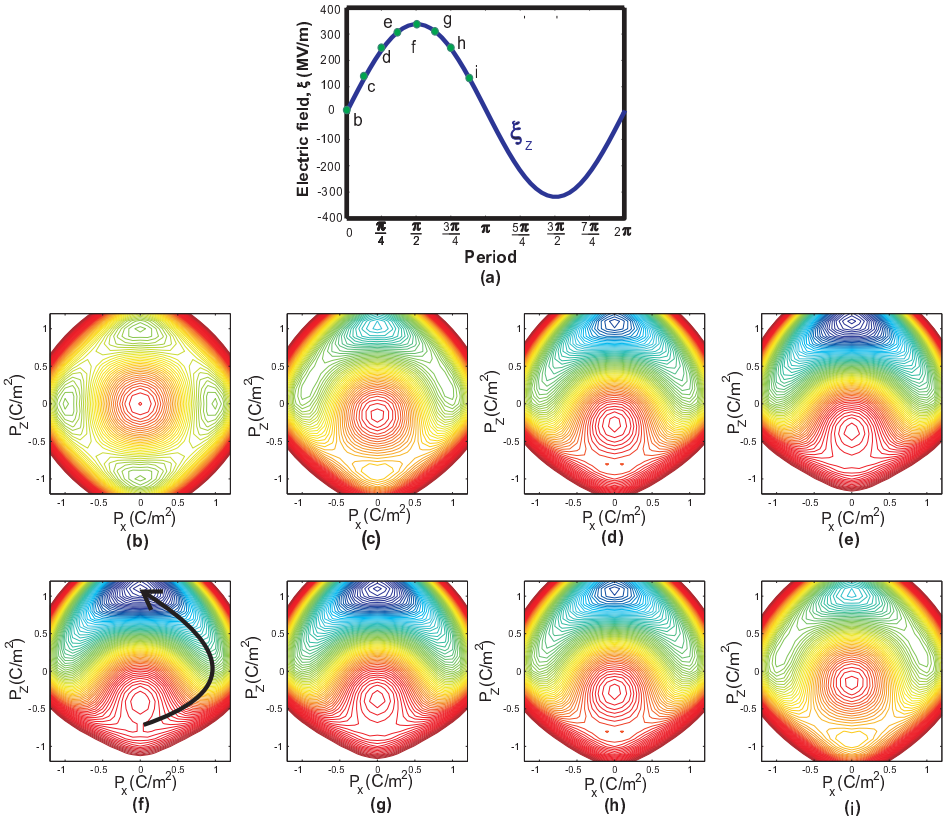

Figure 5.4: Alternating electric field with peak value of $\mathcal{E}_C$= 325 MV/m. The dots on panels (b-i) are spaced within $\frac{\pi}{8}$ intervals of the time period. Each contour plot from (b-i) represents the evolution of energy surface during the corresponding period interval. The ferroelectric switching takes place in a curved path at the peak amplitude interval of $4\,\frac{\pi}{8}$(f).

It is now apparent that for an applied field in particular direction, switching does not take place along a linear path through the paraelectric state but rather follows

a curved path requiring much lower electric field. Because of its curved nature, ferroelectric switching path also has a component in the perpendicular direction to the applied field. The analysis of the switching path suggests that the process can facilitated by applying the electric field in a direction tangential to the path. Based on this finding, we propose an alternative approach to drive a ferroelectric crystal more energy efficiently. (patent pending)

5.5 A model to drive ferroelectric crystal

In a conventional operation of a ferroelectric material, a pair of electric contacts are attached on the faces of the ferroelectric crystal (Fig. 5.5(a)) to apply alternating electric field. However, as it is now evident that the switching takes place with a component in the perpendicular direction too, we propose the addition of an assisting electric field component in the perpendicular direction by attaching another set of contacts on the corresponding faces (Fig. 5.5(b)). This additional alternating electric field will serve as a guide to the curved path of switching process and as a result, the ferroelectric switching can be achieved at a lower magnitude of electric field. Nevertheless, since the perpendicular component of the curved switching path alternate polarity during the half period, the perpendicular assisting field has to be applied accordingly in a manner that it finishes the half cycle during the quarter period of the main component of the electric field.

Such a ferroelectric switching with a lower magnitude of electric field essentially implies lower hysteresis loss of the crystal which in turn results in lower dielectric dissipation in the material.

In addition, achievement of the identical piezoelectric response with a lower field also implies a significant reduction in the power required to drive the crystal as the applied current, $I{=}\mathcal{E}^2/R$ where R is the ohmic resistance of the material. Thus, ferroelectric switching with the proposed method can significantly improve the energy efficiency along with reduced overheating issue.

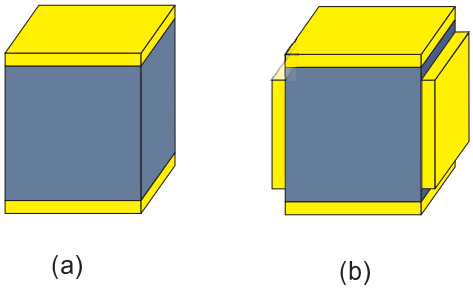

Figure 5.5: (a) Electric contacts (yellow plates) are applied in two opposite sides to apply electric field in one direction (b) Proposed method of applying electric contacts in a manner that electric field can be applied from 2 different direction

The curved nature of the switching path and proposed method of electric field from two direction allow several ways of achieving the ferroelectric switching phenomenon. Figure 5.6 presents one such particular example. Here, two sets of alternating electric field has been applied with one of them (main component with a peak of 163 MV/m) in the direction of desired switching (Z crystallographic direction) and another one with same magnitude (peak of 163 MV/m) but with a phase shift of 90^0 as a perpendicular assisting component in X crystallographic direction. Such an electric field can be applied from identical source which makes the process much simpler in comparison to process that involves several sources of electric field. Ferroelectric switching to

the desired spontaneous polarization state takes place at a field of 163 MV/m in the polarized direction and null in the perpendicular assisting direction (Fig. 5.6(f)). It is thus confirmed that the ferroelectric switching with the proposed model can take place with an coercive field significantly lower in magnitude than the field that would require in achieving the same effect with a one directional field only. Since, hysteresis loss of ferroelectric is depends on the coercive field of materials, reducing the coercive field thus cause the shrinkage of the area of the hysteresis loop (Fig. 5.7 with less hysteresis loss. As a result, much less dielectric dissipation of the ferroelectric material is ensured when a two dimensional electric field is applied.

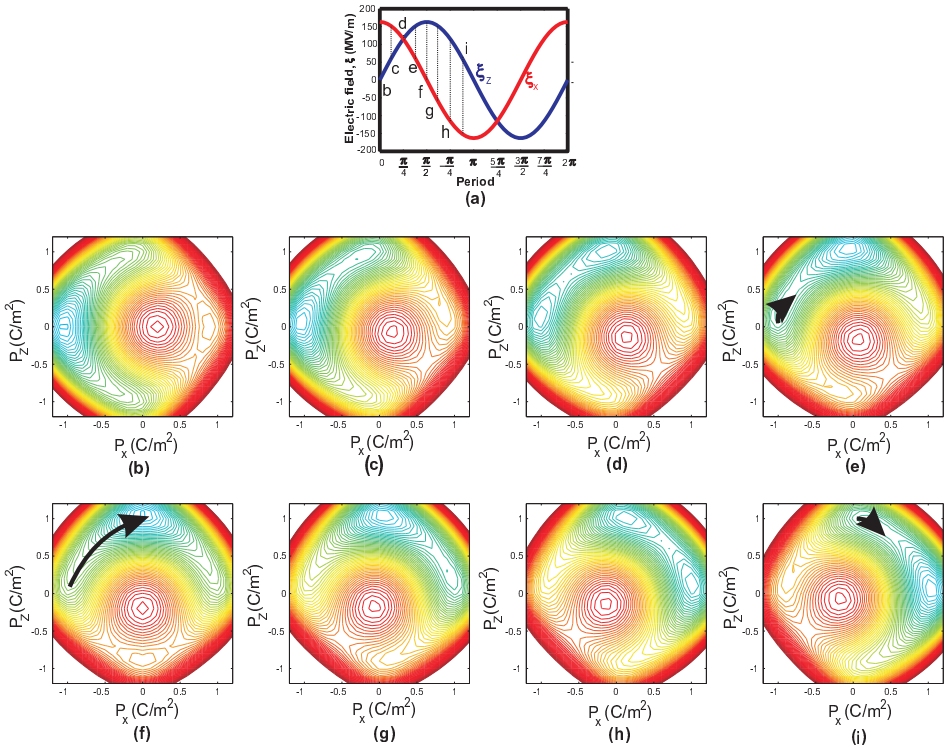

Figure 5.6: (a) The applied alternating electric field based on the proposed model where the main component applied in the direction of switching has a peak of 163 MV/m and the assisting field has a peak of 115 MV/m. The panels (b-i) are spaced within $\frac{\pi}{8}$ intervals of the time period. Evolution of energy surface with alternating electric field from two directions is illustrated from (b-i)

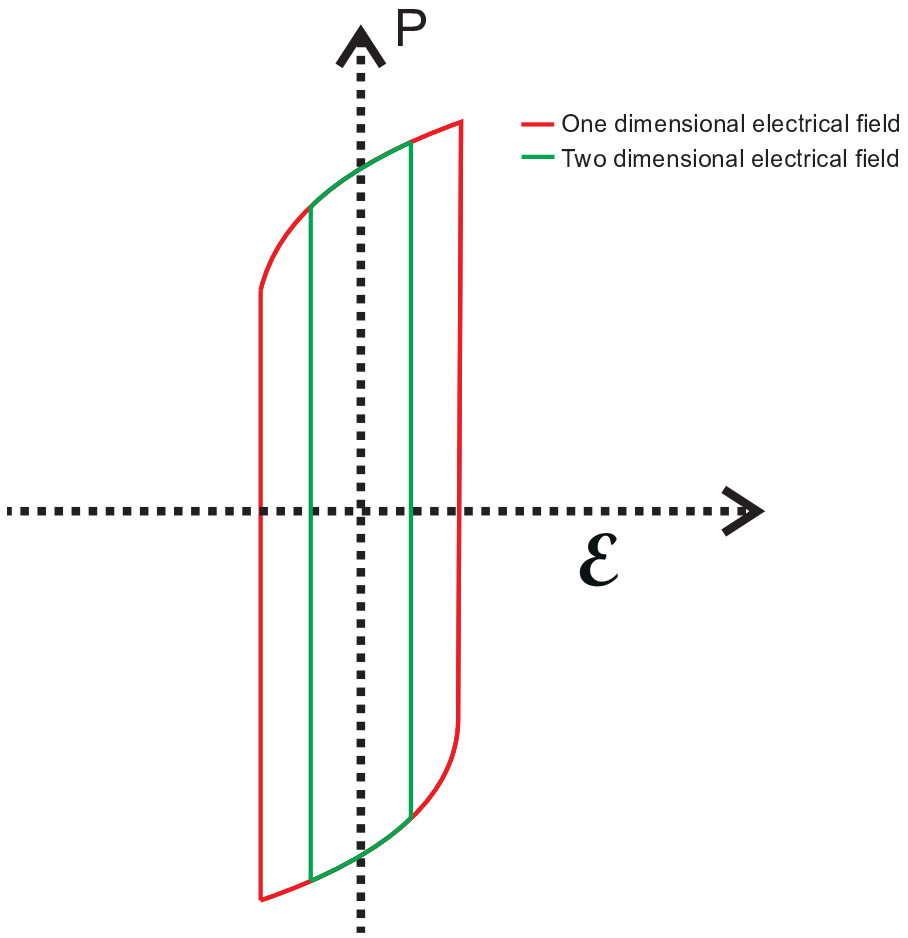

Figure 5.7: Application of an two dimensional electric field results in a much lower hysteresis area (green color) compared to the hysteresis area obtain by an one dimensional field(red color)

Chapter 6

Conclusions

In this work, we first presented a module that extends the capability of `WIEN2k` (all-electron density functional package) to the calculation of polarization using the Berry phase approach. The accuracy of calculations was verified using a model of non-interacting noble atoms. We applied the approach to calculation of spontaneous polarization and Born effective charge of some well characterized perovskite crystals, sodium chloride and zinc-blende structures. Obtained results agree well with alternative calculations and experimental data. The module serves as an useful tool for studies involving ferroelectric materials within all electron full-potential linearized augmented plane wave framework.

Then, with the goal of establishing a basis for screening of potential ferroelectric materials, we performed a domain wall motion study in $BaTiO_3$. There, we have shown that the polarization switching is a non-concurrent process which results in the formation of domain walls. Our study has captured two distinct phases (nucleation and propagation) of the domain wall motion at the microscopic level. Results

of the calculations suggest that the nucleation of domain walls requires overcoming of an energetic barrier, which is much higher than the one corresponding to the propagation phase. The intrinsic coercive field was computed based on the total energy vs. polarization profile. The coercive field calculated in the framework of Landau-Devonshire model is comparable to the results obtained with a more elaborate theory that includes effects of the domain wall motion. It is well known that, ferroelectric switching is strongly influenced by the the domain wall motion. The study of such motion will serve as a basis for future studies involving the application based screening of ferroelectric materials using first principle methods.

Finally, we performed a study on finding the optimum switching path for polarization reversal between two opposite spontaneous polarization states. Based on the findings, we proposed an optimized method of applying electric field to the ferroelectric crystal that can drive them with much lower value of field and thus, much lower dielectric dissipation. Application of the proposed method experimentally to the existing ferroelectric materials during MRgFUS operation will significantly assist in reducing the current challenge involving the thermal build up during the treatment.

Bibliography

[1] J.E Kennedy, GR. Ter-Haar, and D. Cranston. High intensity focused ultrasound: surgery of the future ? *Br. J. Radiol.*, **76**:590–599, 2003.

[2] F. A. Jolesz and K. H. Hynynen. Introduction. In *MRI-Guided Focused Ultrasound Surgery*, chapter 1, pages 1–4.

[3] V. Rieke and K. B. Pauly. MR thermometry. *J. Magn. Reson. Imaging*, **27(2)**:376–390, 2008.

[4] Brigham Department of Radiology and Boston Massachusetts Women's Hospital, Harvard Medical School. http://brainchemist.wordpress.com/2010/11/09/mri-guided-focused-ultrasound-surgery-radiology-brigham-and-womens-hospital-harvard.

[5] K. H. Hynynen. Fundamental principles of therapeutic ultrasound. In *MRI-Guided Focused Ultrasound Surgery*, chapter 2, pages 5–23.

[6] P. L. Carson. Biomedical ultrasonics. *J. Clin. Ultrasound*,**6(2)**:126–127, 1978.

[7] J. W. Hunt. Principles of Ultrasound used for Hyperthermia. In StanleyB.

Field and Cafiero Franconi, editors, *Physics and Technology of Hyperthermia*, volume 127, pages 354–389. Springer Netherlands, 1987.

[8] K. Hynynen. Biophysics and technology of Ultrasound Hyperthermia. In Michel Gautherie, editor, *Methods of External Hyperthermic Heating*, Clinical Thermology, pages 61–115. Springer Berlin Heidelberg, 1990.

[9] A. Simmon. http://www.genesis.net.au/ ajs/projects/medical_physics/ ultrasound/index.html.

[10] M. Takasaki, Y. Maruyama, and T. Mizuno. Resonance Frequency Tracing System for Langevin Type Ultrasonic Transducers. In *Mechatronics and Automation, 2007. ICMA 2007. International Conference on*, pages 3817 –3822, aug. 2007.

[11] W. R. Hendee and E. R. Ritenour. Ultrasound transducers. In *Medical Imaging Physics*, pages 317–330. John Wiley & Sons, Inc., 2003.

[12] J. Curie, P. Curie. Dveloppement, par pression, de l'lectricit polaire dans les cristaux hmidres faces inclines. *Comptes Rendus (France)*, **91**:294–295, 1880.

[13] G. Lippmann Principe de la conservation de l'lectricit. *Ann de Chemie e de Physique(5 serie)*,**24**:145, 1881.

[14] J. Curie, P. Curie. Developpement par pression, de l' electricit e polaire dans les cristaux h emi edres a faces inclin ees. *Comptes Rendus (France)*, **93**:1137–1140, 1881.

[15] A. L. Kholkin, N. A. Pertsev, and A. V. Goltsev. Piezoelectricity and crystal symmetry. In A. Safari and E.K. Akdogan, editors, *Piezoelectric and Acoustic Materials for Transducer Applications*, pages 17–38. Springer US, 2008.

[16] Fundamentals of piezoelectricity. In *Piezoelectric Transducers for Vibration Control and Damping*, Advances in Industrial Control, pages 9–35. Springer London, 2006.

[17] K.H. Hardtl. Electrical and mechanical losses in ferroelectric ceramics. *Ceram. Int.*, **8(4)**:121 – 127, 1982.

[18] R. E. Cohen and H. Krakauer. Lattice dynamics and origin of ferroelectricity in $BaTiO_3$: Linearized-augmented-plane-wave total-energy calculations. *Phys. Rev. B*, **42**:6416–6423, 1990.

[19] R. E. Cohen. Origin of ferroelectricity in perovskite oxides. *Nature(London)*, **358**:136–138, 1992.

[20] R. D. King-Smith and D. Vanderbilt. First-principles investigation of ferroelectricity in perovskite compounds. *Phys. Rev. B*, **49**:5828–5844, 1994.

[21] R. E. Cohen. Theory of ferroelectrics: a vision for the next decade and beyond. *J. Phys. Chem. Solids*, **61(2)**:139–146, 2000.

[22] J. Valasek. Piezo-Electric and Allied Phenomena in Rochelle Salt. *Phys. Rev.*, **17**:475–481, 1921.

[23] M. E. Lines and A.M. Glass. *Principles and Applications of Ferroelectrics and Related Materials*. Oxford Classics Series, 2001.

[24] V. Marek. *First-pinciples study of the nonlinear responces of insulators to electric fields:applications to ferroelectric oxides.* PhD thesis, Universite De Liege, 2005.

[25] K. Rabe and P. Ghosez. First-principles studies of ferroelectric oxides. In *Physics of Ferroelectrics*, volume 105 of *Topics in Applied Physics*, pages 117–174. Springer Berlin Heidelberg, 2007.

[26] C. P. Smyth. *Dielectric Behavior and Structure: Dielectric Constant and Loss, Dipole Moment and Molecular Structure.* International chemical series. Xerox University Microfilms, 1975.

[27] E. Heinonen, J. Juuti, and S. Leppvuori. Characterization and modelling of 3d piezoelectric ceramic structures with atila software. *Journal of the European Ceramic Society*, **25(12)**:2467 – 2470, 2005.

[28] T. M. Htike. PZT material properties http://www.scribd.com/doc/34864965/pzt-material-properties

[29] Z. W. Qian, L. Xiong, J. Yu, D. Shao, H. Zhu, and X. Wu. Noninvasive thermometer for HIFU and its scaling. *Ultrasonics*, **44**:e31 – e35, 2006.

[30] J. Coon, A. Payne, and R. Roemer. HIFU treatment time reduction in superficial tumours through focal zone path selection. *Int. J. Hyperther.*, **27(5)**:465–81, 2011.

[31] N. J. McDannold, F. A. Jolesz, and K. H. Hynynen. Determination of the optimal delay between sonications during focused ultrasound surgery in rab-

bits by using MR imaging to monitor thermal build up in vivo. *Radiology*, **211(2)**:419–26, 1999.

[32] F. M. Fennessy and C. M. Tempany. MRI-guided Focused Ultrasound Surgery of Uterine Leiomyomas1. *Academic Radiology*, **12(9)**:1158 – 1166, 2005.

[33] K. Uchino and S. Hirose. Loss mechanisms in piezoelectrics: How to measure different losses separately. *Ultrasonics, Ferroelectrics and Frequency*, **48(1)**:307, 2001.

[34] Y. Chen, Y. Wen, and P. Li. Loss mechanisms in piezoelectric transducers and its response to stress. *Information Acquisition, 2004*, **(50278098)**:213–219, 2004.

[35] S. C. Bhatt and M. Uniyal. Synthesis, Characterization and Dielectric Properties of $K_{1-x}Na_xNbO3$. *International Journal of Materials and Chemistry*, **2(2)**:47–50, August 2012.

[36] A.K. Jonscher. Physical basis of dielectric loss. *Nature*, **253**:717–719, 1975.

[37] M. Lee. Dielectric constant and loss tangent in $LiNbO_3$ crystals from 90 to 147 GHz. *Appl. Phys. Lett.*, **79(9)**:1342, 2001.

[38] D. A. Sanchez, A. Kumar, N. Ortega, R. S. Katiyar, and J. F. Scott. Near-room temperature relaxor multiferroic. *Appl. Phys. Lett.*, **97(20)**:202910, 2010.

[39] K. Uchino, J. H. Zheng, Y. H. Chen, X. H. Du, J. Ryu, Y. Gao, S. Ural, S. Priya, and S. Hirose. Loss mechanisms and high power piezoelectrics. *J. Mater. Sci.*, **41(1)**:217–228, 2006.

[40] N. Yasuda, T. Fuwa, H. Ohwa, Y. Tachi, and Y. Yamashita. The effect of poling and depoling on the dielectric and piezoelectric properties of relaxor ferroelectric solid solution single crystal of $24Pb(In_{1/2}Nb_{1/2})O_3$-$46Pb(Mg_{1/3}Nb_{2/3})O_3$-$30PbTiO_3$. In *Applications of Ferroelectrics (ISAF/PFM), 2011 International Symposium on and 2011 International Symposium on Piezoresponse Force Microscopy and Nanoscale Phenomena in Polar Materials*, pages 1–4, 2011.

[41] J. Zheng and S. Takahashi. Heat generation in multilayer piezoelectric actuators. *Journal of the Americal Ceramic Society*, **79(12)**:3193–98s, 1996.

[42] S.-W. Zhou and C. A. Rogers. Heat Generation, Temperature, and Thermal Stress of Structurally Integrated Piezo-Actuators. *Journal of Intelligent Material Systems and Structures*, **6(3)**:372–379, May 1995.

[43] C. J. Fennie and K. M. Rabe. Magnetic and electric phase control in epitaxial $EuTiO_3$ from first principles. *Phys. Rev. Lett.*, **97**:267602, 2006.

[44] J. H. Lee, L. Fang, E. Vlahos, X. Ke, Y. W. Jung, L. F. Kourkoutis, J.-W. Kim, P. J. Ryan, T. Heeg, M.Roeckerath. A strong ferroelectric ferromagnet created by means of spin-lattice coupling. *Nature*, **466(7309)**:954–958, 2010.

[45] J. W. Bennett and K. M. Rabe. Integration of first-principles methods and crystallographic database searches for new ferroelectrics: Strategies and explorations. *J. Solid State Chem.*, **195**:21–31, 2012.

[46] J. W. Bennett, K. F. Garrity, K. M. Rabe, and D. Vanderbilt. Hexagonal ABC semiconductors as ferroelectrics. *Phys. Rev. Lett.*, **109**:167602, Oct 2012.

[47] T. Nishimatsu, U. V. Waghmare, Y. Kawazoe, and D. Vanderbilt. Fast molecular-dynamics simulation for ferroelectric thin-film capacitors using a first-principles effective hamiltonian. *Phys. Rev. B*, **78**:104104, 2008.

[48] Y. Zhang, J. Hong, B. Liu, and D. Fang. Molecular dynamics investigations on the size-dependent ferroelectric behavior of $BaTiO_3$ nanowires. *Nanotechnology*, **20(40)**:405703, 2009.

[49] J. Padilla, W. Zhong, and D. Vanderbilt. First-principles investigation of 180^0 domain walls in $BaTiO_3$. *Phys. Rev. B*, **53**:R5969–R5973, 1996.

[50] B. Meyer and D. Vanderbilt. *Ab initio* study of ferroelectric domain walls in $PbTiO_3$. *Phys. Rev. B*, **65**:104111, 2002.

[51] X. Wu and D. Vanderbilt. Theory of hypothetical ferroelectric superlattices incorporating head-to-head and tail-to-tail 180 degree domain walls. *Phys. Rev. B*, **73**:020103, 2006.

[52] C. Li, K. C. K. Soh, and P. Wu. Formability of ABO_3 perovskites. *Journal of alloys and compounds*, **372**(1):40–48, 2004.

[53] H. Zhang, N. Li, K. Li, and D. Xue. Structural stability and formability of ABO_3-type perovskite compounds. *Acta Crystallographica Section B: Structural Science*, **63(6)**:812–818, 2007.

[54] C. Li, X. Lu, W. Ding, L. Feng, Y. Gao, and Z. Guo. Formability of ABX_3 (X= F, Cl, Br, I) halide perovskites. *Acta Crystallographica Section B: Structural Science*, **64(6)**:702–707, 2008.

[55] A. Kumar, A.S. Verma, and S.R. Bhardwaj. Prediction of formability in perovskite-type oxides. *Open Applied Physics Journal*, **1**:11–19, 2008.

[56] P. Ghosez. *First-principles study of the dielectric and dynamical properties of Barium titanate*. PhD thesis, Universite Catholiqe De Louvain, 1997.

[57] M. Born and R. Oppenheimer. Zur quantentheorie der molekeln. *Annalen der Physik*, **389(20)**:457–484, 1927.

[58] D. R. Hartree. The wave mechanics of an atom with a non-coulomb central field. part i. theory and methods. *Mathematical Proceedings of the Cambridge Philosophical Society*, **24**:89–110, 1928.

[59] R. Resta and D. Vanderbilt. Computational physics. pages 50. Cambridge University Press, 2007.

[60] V. Fock. Nherungsmethode zur lsung des quantenmechanischen mehrkrper-problems. *Zeitschrift fr Physik*, **61(1-2)**:126–148, 1930.

[61] N. Kryloff. *Mem. des Sci. Math. fasc*, XLIX, 1931.

[62] K. Hohenemser. *Die Methoden zur Angenaherten Losung von Eigenwertproblemen in der Elastokinetic*. Springer, Berlin, 1932.

[63] Kemble. *Rev. Mod. Phys*, **1**:206, 1929.

[64] R. Resta and D. Vanderbilt. Computational physics. pages 94. Cambridge University Press, 2007.

[65] P. Hohenberg and W. Kohn. Inhomogeneous electron gas. *Phys. Rev.*, 136(3B):B864, 1964.

[66] W. Kohn and L. J. Sham. Self-consistent equations including exchange and correlation effects. *Phys. Rev.*, **140**:A1133–A1138, 1965.

[67] S. Cottenier. Density Functional Theory and the family of (L) APW-methods: a step-by-step introduction. *Instituut voor Kern-en Stralingsfysica, KU Leuven, Belgium*, 2002.

[68] N. Sai. *First-pinciples modeling of structural and electronic properties in ferroelectric compounds*. PhD thesis, New Brusnwick Rutgers, The State University of New Jersey, 2002.

[69] J. Kohanoff. *Electronic structure calculations for solids and molecules: theory and computational methods*. Cambridge University Press, 2006.

[70] PA. Dirac. *Note on exchange phenomena in the Thomas atom*. Cambridge University Press, 1930.

[71] M. Stadele, M. Moukara, J. A. Majewski, P. Vogl, and A. Gorling. Exact exchange kohn-sham formalism applied to semiconductors. *Phys. Rev. B*, **59**:10031–10043, 1999.

[72] D. M. Bylander and L. Kleinman. Good semiconductor band gaps with a modified local-density approximation. *Phys. Rev. B*, **41**:7868–7871, 1990.

[73] A. D. Becke. A new mixing of Hartree-Fock and local density-functional theories. *J. Chem. Phys.*, **98**:1372, 1993.

[74] F. Bechstedt, F. Fuchs, and G. Kresse. Ab-initio theory of semiconductor band structures: New developments and progress. *Phys. Status Solidi B*, **246**:1877–1892, 2009.

[75] S.J. Ahmed, J. Kivinen, B. Zaporzan, L. Curiel, S. Pichardo, and O. Rubel. BerryPI: A software for studying polarization of crystalline solids with WIEN2k density functional all-electron package. *Comput. Phys. Commun.*, **184(3)**:647–651, 2012.

[76] K. M. Rabe. Computational materials science: Think locally, act globally. *Nat. Mater.*, **1(3)**:1122–1476, 2002.

[77] R. F. Service. Materials scientists look to a data-intensive future. *Science*, **335**:1434–1435, 2012.

[78] R. D. King-Smith and D. Vanderbilt. Theory of polarization of crystalline solids. *Phys. Rev. B*, **47**:1651–1654, 1993.

[79] R. Resta, M. Posternak, and A. Baldereschi. Towards a quantum theory of polarization in ferroelectrics: The case of $KNbO_3$. *Phys. Rev. Lett.*, **70(7)**:1010–1013, 1993.

[80] R. Resta. Macroscopic polarization in crystalline dielectrics: the geometric phase approach. *Rev. Mod. Phys.*, **66**:899–915, 1994.

[81] F. Bernardini, V. Fiorentini, and D. Vanderbilt. Spontaneous polarization and piezoelectric constants of III-V nitrides. *Phys. Rev. B*, **56(16)**:R10024–R10027, October 1997.

[82] R. Resta and D. Vanderbilt. Theory of polarization: A modern approach. In *Physics of Ferroelectrics*, volume 105 of *Topics in Applied Physics*, pages 31–68. Springer Berlin Heidelberg, 2007.

[83] G. Sághi-Szabó, R. E. Cohen, and H. Krakauer. First-Principles Study of Piezoelectricity in $PbTiO_3$. *Phys. Rev. Lett.*, **80(19)**:4321–4324, 1998.

[84] D. Vanderbilt. Berry-phase theory of proper piezoelectric response. *Journal of Physics and Chemistry of Solids*, **61**:147 – 151, 2000.

[85] X. Gonze, J. M. Beuken, R. Caracas, F. Detraux, M. Fuchs, G. M. Rignanese, L Sindic, M Verstraete, G Zerah, F Jollet, M Torrent, A Roy, M Mikami, Ph. Ghosez, J.-Y. Raty, and D C Allan. First-principles computation of material properties: the ABINIT software project. *Comp. Mat. Sci*, **25(3)**:478–492, 2002.

[86] G. Kresse and J. Furthmller. Efficiency of ab-initio total energy calculations for metals and semiconductors using a plane-wave basis set. *Comp. Mat. Sci.*, **6**:15–50, 1996.

[87] P. Blaha, K. Schwarz, G. K. H. Madsen, D. Kvasnicka, and J. Luitz. *WIEN2K, An Augmented Plane Wave + Local Orbitals Program for Calculating Crystal Properties*. Karlheinz Schwarz, Techn. Universität Wien, Austria, 2001.

[88] J. Kunes, R. Arita, P. Wissgott, A. Toschi, H. Ikeda and K. Held. Wien2wannier: From linearized augmented plane waves to maximally localized wannier functions. *Computer Physics Communications*, **181(11)**:1888 – 1895, 2010.

[89] L.D Landau and E.M Lifshitz *Electrodynamics of Continious Media.* Pergamon, Oxford, 1984.

[90] R. Resta. Theory of the electric polarization in crystals. *Ferroelectrics*, **136(1)**:51–55, 1992.

[91] M.V. Berry. Quantal phase factors accompanying adiabatic changes. *P. Roy. Soc. Lond. A*, **392(45)**:52109, 1984.

[92] X. Wang. *First-principles calculation of dynamical properties of insulators in finite electric fields and anomalous hall conductivity of ferromagnets based on Berry phase approach.* PhD thesis, New Brunswick Rutgers, The State University of New Jersey, 2007.

[93] E.I. Blount newblock *Solid State Phys.*, **13**:305, 1962.

[94] J. P. Perdew, K. Burke, and M. Ernzerhof. Generalized gradient approximation made simple. *Phys. Rev. Lett.*, **77**:3865–3868, 1996.

[95] G. Shirane F. Jona. *Ferroelectric Crystals*, Dover, New York, 1993.

[96] G. H. Kwei, a. C. Lawson, S. J. L. Billinge, and S. W. Cheong. Structures of the ferroelectric phases of Barium titanate. *The Journal of Physical Chemistry*, **97(10)**:2368–2377, 1993.

[97] A.W. Hewat. Cubic-tetragonal-orthorhombic-rhombohedral ferroelectric transitions in perovskite Potassium Niobate: Neutron powder profile refinement of the structures. *Journal of Physics C: Solid State Physics*, **6**:2559, 1973.

[98] C. Hartwigsen, S. Goedecker, and J. Hutter. Relativistic separable dual-space Gaussian pseudopotentials from H to Rn. *Phys. Rev. B*, **58**:3641–3662, 1998.

[99] M. Fechner, S. Ostanin, and I. Mertig. Effect of the surface polarization in polar perovskites studied from first principles. *Phys. Rev. B*, **77**:094112, 2008.

[100] J. J. Wang, F. Y. Meng, X. Q. Ma, M. X. Xu, and L. Q. Chen. Lattice, elastic, polarization, and electrostrictive properties of $BaTiO_3$ from first-principles. *J. Appl. Phys.*, **108(3)**:034107, 2010.

[101] C.Z. Wang, R. Yu, and H. Krakauer. Born effective charges, dielectric constants, and lattice dynamics of $KNbO_3$. *Ferroelectrics*, **194(1)**:97–107, 1997.

[102] HH. Wieder. Electrical Behavior of Barium Titanate Single Crystals at Low Temperatures. *Phys. Rev.*, **99(4)**:1161–1165, 1955.

[103] W. Kleemann, F J Schäfer, and M. D. Fontana. Crystal optical studies of spontaneous and precursor polarization in $KNbO_3$. *Phys. Rev. B*, **30(3)**:1148–1154, 1984.

[104] V. G. Gavrilyachenko. *Sov. Phys. Solid State*, **12**:1203, 1970.

[105] Ph. Ghosez, J.-P. Michenaud, and X. Gonze. Dynamical atomic charges: The case of ABO_3 compounds. *Phys. Rev. B*, **58(10)**:6224–6240, 1998.

[106] M. Born and K. Huang. *Dynamical Theory of Crystal Lattices.* University Press, Oxford, 1968.

[107] T. Sengstag, N. Binggeli, and A. Baldereschi. Anomalies in the pressure

dependence of the effective charge in cubic semiconductors. *Phys. Rev. B*, **52**(12):R8613—-R8616, 1995.

[108] A. Shukla. Ab initio Hartree-Fock born effective charges of LiH, LiF, LiCl, NaF, and NaCl. *Phys. Rev. B*, **61**:13277–13282, 2000.

[109] T.R. Koehler, A.R. Bishop, J.A. Krumhansl, and J.R Schrieffer. Molecular dynamics simulation of a model for (one-dimensional) structural phase transitions. *Solid State Commun.*, **17(12)**:1515 – 1519, 1975.

[110] Y. H. Shin, V. R. Cooper, I. Grinberg, and A. M. Rappe. Development of a bond-valence molecular-dynamics model for complex oxides. *Phys. Rev. B*, **71**:054104, 2005.

[111] J. Paul, T. Nishimatsu, Y. Kawazoe, and U. V. Waghmare. Ferroelectric phase transitions in ultrathin films of $BaTiO_3$. *Phys. Rev. Lett.*, **99**:077601, 2007.

[112] Y. H. Shin, I. Grinberg, I. W. Chen, and A. M. Rappe. Nucleation and growth mechanism of ferroelectric domain-wall motion. *Nature*, **449**:881–884, 2007.

[113] J. Paul, T. Nishimatsu, Y. Kawazoe, and U. V. Waghmare. Polarization switching in epitaxial films of $BaTiO_3$: A molecular dynamics study. *Appl. Phys. Lett.*, **93(24)**:242905, 2008.

[114] S. Poykko and D. J. Chadi. Ab initio study of 180^0 domain wall energy and structure in $PbTiO_3$. *Appl. Phys. Lett.*, **75(18)**:2830–2832, 1999.

[115] S. P. Beckman, X. Wang, K. M. Rabe, and D. Vanderbilt. Ideal barriers to

polarization reversal and domain-wall motion in strained ferroelectric thin films. *Phys. Rev. B*, **79**:144124, 2009.

[116] L. D. Landau. *Phys. Z. Sowjun.*, **11**:545, 1937.

[117] L. D. Landau. *Zh. Eksp. Teor. Fiz*, **7**:627, 1937.

[118] A.F. Devonshire. Xcvi. theory of Barium titanate. *Philos. Mag.*, **40(309)**:1040–1063, 1949.

[119] A.F. Devonshire. Cix. theory of Barium titanate-part ii. *Philos. Mag.*, **42(333)**:1065–1079, 1951.

[120] A.F. Devonshire. Theory of ferroelectrics. *Adv. Phys.*, **3(10)**:85–130, 1954.

[121] J. C. V. Perez. *Characterization and modeling of ferroelectric materials for high pressure, high temperature applications*. PhD thesis, University of California Los Angeles, 2013.

[122] P. Chandra and P. Littlewood. A landau primer for ferroelectrics. In *Physics of Ferroelectrics*, volume 105 of *Topics in Applied Physics*, pages 69–116. Springer Berlin Heidelberg, 2007.

[123] S. T.-McKinstry. Crystal chemistry of piezoelectric materials. In Ahmad Safari and E.Koray Akdogan, editors, *Piezoelectric and Acoustic Materials for Transducer Applications*, pages 39–56. Springer US, 2008.

[124] M. Taherinejad, D. Vanderbilt, P. Marton, V. Stepkova, and J. Hlinka. Bloch-type domain walls in rhombohedral $BaTiO_3$. *Phys. Rev. B*, **86**:155138, 2012.

[125] B. Meyer and D. Vanderbilt. Ab initio study of ferroelectric domain walls in $PbTiO_3$. *Phys. Rev. B*, **65**:104111, 2002.

[126] D. Lee, R. K. Behera, P. Wu, H. Xu, Y. L. Li, S. B. Sinnott, S. R. Phillpot, L. Q. Chen, and V. Gopalan. Mixed bloch-neel-ising character of 180 ferroelectric domain walls. *Phys. Rev. B*, **80**:060102, 2009.

[127] R. K. Behera, C.-W. Lee, D. Lee, A. N. Morozovska, S. B. Sinnott, A. Asthagiri, V. Gopalan, and S. R. Phillpot. Structure and energetics of 180 domain walls in $PbTiO_3$ by density functional theory. *J. Phys.: Condens. Matter*, **23(17)**:175902, 2011.

[128] P Marton, I Rychetsky, and J Hlinka. Domain walls of ferroelectric $BaTiO_3$ within the ginzburg-landau-devonshire phenomenological model. *Phys. Rev. B*, **81(14)**:144125, 2010.

[129] D. I. Bilc, R. Orlando, R. Shaltaf, G. M. Rignanese, Jorge Íñiguez, and Ph. Ghosez. Hybrid exchange-correlation functional for accurate prediction of the electronic and structural properties of ferroelectric oxides. *Phys. Rev. B*, **77(16)**:165107, 2008.

[130] W. Kohn and L. J. Sham. Self-consistent equations including exchange and correlation effects. *Phys. Rev.*, **140**:A1133–A1138, 1965.

[131] U. V. Barth and L. Hedin. A local exchange-correlation potential for the spin polarized case. *J. Phys. C*, **5(13)**:1629, 1972.

[132] O. Gunnarsson and B. I. Lundqvist. Exchange and correlation in atoms,

molecules, and solids by the spin-density-functional formalism. *Phys. Rev. B*, **13**(10):4274, 1976.

[133] L. He and D. Vanderbilt. First-principles study of oxygen-vacancy pinning of domain walls in $PbTiO_3$. *Phys. Rev. B*, **68**:134103, 2003.

[134] G. Shirane, H. Danner, and R. Pepinsky. Neutron diffraction study of orthorhombic $BaTiO_3$. *Phys. Rev.*, **105**:856–860, 1957.

[135] S. Ducharme, V. M. Fridkin, A. V. Bune, S. P. Palto, L. M. Blinov, NN Petukhova, and SG Yudin. Intrinsic ferroelectric Coercive field. *Phys. Rev. Lett.*, **84(1)**:175–178, 2000.

[136] M. E. Lines and A. M. Glass. *Principles and applications of ferroelectrics and related materials*. Oxford University Press, 1977.

[137] S. Kim, V. Gopalan, and A. Gruverman. Coercive fields in ferroelectrics: A case study in Lithium Niobate and Lithium Tantalate. *Appl. Phys. Lett.*, **80(15)**:2740–2742, 2002.

[138] W. J. Merz. Switching time in ferroelectric $BaTiO_3$ and its dependence on crystal thickness. *J. Appl. Phys.*, **27(8)**:938–943, 1956.

[139] I. Lefkowitz and T. Mitsui. Effect of gamma-ray and pile irradiation on the Coercive field of $BaTiO_3$. *J. Appl. Phys.*, **30(2)**:269–269, 1959.

[140] M. Tanaka and H. Goro. Electron optical studies of barium titanate single crystal films. *J. Phys. Soc. Jpn.*, **19**:954, 1964.